The Y-type brown dwarfs: estimates of mass and age from new astrometry, homogenized photometry, and near-infrared spectroscopy

K. Leggett, Pascal Tremblin, T. Esplin, K. Luhman, Caroline Morley

The Astrophysical Journal, 842:118 (25pp), 2017 June 20 https://doi.org/10.3847/1538-4357/aa6fb5

The Y-type Brown Dwarfs: Estimates of Mass and Age from New Astrometry, Homogenized Photometry, and Near-infrared Spectroscopy

S. K. Leggett[1], P. Tremblin[2], T. L. Esplin[3], K. L. Luhman[3,4], and Caroline V. Morley[5]
[1] Gemini Observatory, Northern Operations Center, 670 N. A'ohoku Place, Hilo, HI 96720, USA; sleggett@gemini.edu
[2] Maison de la Simulation, CEA-CNRS-INRIA-UPS-UVSQ, USR 3441, Centre d'étude de Saclay, F-91191 Gif-Sur-Yvette, France
[3] Department of Astronomy and Astrophysics, The Pennsylvania State University, University Park, PA 16802, USA
[4] Center for Exoplanets and Habitable Worlds, The Pennsylvania State University, University Park, PA 16802, USA
[5] Harvard-Smithsonian Center for Astrophysics, Harvard University, Cambridge, MA 02138, USA
Received 2017 January 5; revised 2017 April 10; accepted 2017 April 11; published 2017 June 21

Abstract

The survey of the mid-infrared sky by the *Wide-field Infrared Survey Explorer* (*WISE*) led to the discovery of extremely cold, low-mass brown dwarfs, classified as Y dwarfs, which extend the T class to lower temperatures. Twenty-four Y dwarfs are known at the time of writing. Here we present improved parallaxes for four of these, determined using *Spitzer* images. We give new photometry for four late-type T and three Y dwarfs and new spectra of three Y dwarfs, obtained at Gemini Observatory. We also present previously unpublished photometry taken from *HST*, ESO, *Spitzer*, and *WISE* archives of 11 late-type T and 9 Y dwarfs. The near-infrared data are put onto the same photometric system, forming a homogeneous data set for the coolest brown dwarfs. We compare recent models to our photometric and spectroscopic data set. We confirm that nonequilibrium atmospheric chemistry is important for these objects. Nonequilibrium cloud-free models reproduce well the near-infrared spectra and mid-infrared photometry for the warmer Y dwarfs with $425 \leqslant T_{\rm eff}$ (K) $\leqslant 450$. A small amount of cloud cover may improve the model fits in the near-infrared for the Y dwarfs with $325 \leqslant T_{\rm eff}$ (K) $\leqslant 375$. Neither cloudy nor cloud-free models reproduce the near-infrared photometry for the $T_{\rm eff} = 250$ K Y dwarf W0855. We use the mid-infrared region, where most of the flux originates, to constrain our models of W0855. We find that W0855 likely has a mass of 1.5–8 Jupiter masses and an age of 0.3–6 Gyr. The Y dwarfs with measured parallaxes are within 20 pc of the Sun and have tangential velocities typical of the thin disk. The metallicities and ages we derive for the sample are generally solar-like. We estimate that the known Y dwarfs are 3 to 20 Jupiter-mass objects with ages of 0.6–8.5 Gyr.

Key words: brown dwarfs – molecular processes – stars: atmospheres

Supporting material: machine-readable table

1. Introduction

Brown dwarfs are stellar-like objects with a mass too low for stable nuclear fusion. During the first gigayear of a brown dwarf's life, the luminosity decreases by a factor of ∼100, and 1–73 Jupiter-mass brown dwarfs cool to effective temperatures ($T_{\rm eff}$) of ∼200–2000 K (Baraffe et al. 2003; Saumon & Marley 2008). As photometric sky surveys are executed at longer wavelengths and with larger mirrors, fainter and cooler brown dwarfs are identified. Most recently, the *Wide-field Infrared Survey Explorer* (*WISE*; Wright et al. 2010) revealed a population with $250 \lesssim T_{\rm eff}$ (K) $\lesssim 500$, and these have been classified as Y dwarfs (Cushing et al. 2011; Kirkpatrick et al. 2012). The Y dwarfs are an extension of the T-type brown dwarfs, which typically have $500 \lesssim T_{\rm eff}$ (K) $\lesssim 1300$ (e.g., Golimowski et al. 2004; Leggett et al. 2009, 2012).

Significantly, even for the predominantly isolated brown dwarfs in the solar neighborhood, the fundamental parameters mass and age can be estimated if models can be fit to observations and $T_{\rm eff}$ and surface gravity g are constrained. Evolutionary models show that g constrains mass, because the radii of brown dwarfs do not change significantly after about 200 Myr and are within 25% of a Jupiter radius (Burrows et al. 1997). Also, the cooling curves as a function of mass are well understood, so $T_{\rm eff}$ combined with g constrains age (Saumon & Marley 2008).

Models of brown dwarf atmospheres have advanced greatly in recent years. Opacities have been updated for CH_4, H_2, and NH_3 (Yurchenko et al. 2011; Saumon et al. 2012; Yurchenko & Tennyson 2014). Models that include nonequilibrium chemistry driven by vertical gas transport are available (Tremblin et al. 2015, hereafter T15), as are models that include sedimentation by various species, which is clouds (Morley et al. 2012, 2014, hereafter M12 and M14). The models are accurate enough that the physical parameters of the brown dwarf atmospheres can be constrained by comparing the observed output energy of the brown dwarf, in the form of a flux-calibrated spectral energy distribution (SED), to synthetic colors and spectra. This paper enhances the number and quality of Y dwarf SEDs in order to improve our understanding of this cold population. We do this by presenting new photometry and spectra and improved trigonometric parallaxes.

We present new near-infrared spectra for three Y dwarfs obtained with the Gemini near-infrared spectrograph (GNIRS; Elias et al. 2006) and the Gemini imager and spectrometer FLAMINGOS-2 (Eikenberry et al. 2004). We also present new infrared photometry of late-type T and Y dwarfs, obtained with the Gemini observatory near-infrared imager (NIRI; Hodapp et al. 2003) and previously unpublished near- and mid-infrared photometry of late-type T and Y dwarfs taken from data archives. The near-infrared archive photometry is either on the Mauna Kea Observatories (MKO) system (Tokunaga & Vacca 2005) or on the *Hubble Space Telescope (HST)* WFC3 system.

We derive transformations between these two systems and use these to produce a sample of late-T and Y-type dwarfs with single-system photometry. We also present improved parallaxes for four Y dwarfs using *Spitzer* images.

Our new data set is large enough that trends and outliers can be identified. We compare color–color and color–magnitude plots, and near-infrared spectra, to available models. The Y dwarf atmospheric parameters $T_{\rm eff}$, g, and metallicity are constrained, and mass and age are estimated. We also compare models to the photometric SED of the coolest known brown dwarf, WISE J085510.83−071442.5 (Luhman 2014, hereafter W0855) and constrain the properties of this extreme example of the known Y class.

In Section 2 we set the context of this work by illustrating how the shape of synthetic Y dwarf SEDs vary as model parameters are changed. We show the regions of the spectrum sampled by the filters used in this work, and we demonstrate the connection between luminosity, temperature, mass, and age as given by evolutionary models. In Section 3 we describe the model atmospheres used in this work. Section 4 presents the new GNIRS and FLAMINGOS-2 spectra and the new NIRI photometry, and Section 5 presents the previously unpublished photometry extracted from data archives; Section 6 gives transformations between the MKO and WFC3 photometric systems. New parallaxes and proper motions are given in Section 7. Section 8 compares models to the photometric data set, which allows us to estimate some of the Y dwarf properties and also allows us to select a preferred model type for a comparison to near-infrared spectra, which we present in Section 9. Section 10 combines our results to give final estimates of atmospheric and evolutionary parameters for the sample. Our conclusions are given in Section 11.

2. SEDs and Filter Bandpasses

This work focuses on observations and models of Y dwarfs. Figure 1 shows synthetic spectra for a Y dwarf with $T_{\rm eff} = 400$ K, generated from T15 models. The flux emerges through windows between strong absorption bands of primarily CH_4, H_2O, and NH_3 (e.g., M14, their Figure 7). The four panels demonstrate the effect of varying the atmospheric parameters. Near- and mid-infrared filter bandpasses used in this work are also shown.

Figure 1 shows that for a Y dwarf with $T_{\rm eff} \sim 400$ K, changes in $T_{\rm eff}$ of 25 K have large, a factor of ∼2, effects on the absolute brightness of the near-infrared spectrum at all of *YJH*; the flux in the [4.5] bandpass changes by 15%. An increase in metallicity or a decrease in surface gravity g changes the slope of the near-infrared spectrum, brightening the Y and J flux while having only a small effect on H. An increase in metallicity [*m/H*] of 0.2 dex increases the *YJ* flux by 20%–30% and decreases the [4.5] flux by 40%. An increase in gravity g (cm s^{-2}) of 0.5 dex decreases the *YJ* and [4.5] flux by about 15%. Finally, an increase in the eddy diffusion coefficient K_{zz} (cm^2 s^{-1}, the chemical mixing parameter; see Section 3) from 10^6 to 10^8 increases the *YJK* flux by 15% while decreasing the [4.5] flux by 50%. The parameter γ is discussed in Section 3.

The near-infrared spectra of Y dwarfs are therefore expected to be sensitive to all of the atmospheric parameters and especially sensitive to $T_{\rm eff}$. The shape and brightness of the near-infrared spectrum combined with the [4.5] flux can usefully constrain a Y dwarf's atmospheric parameters. We test this in Section 9.

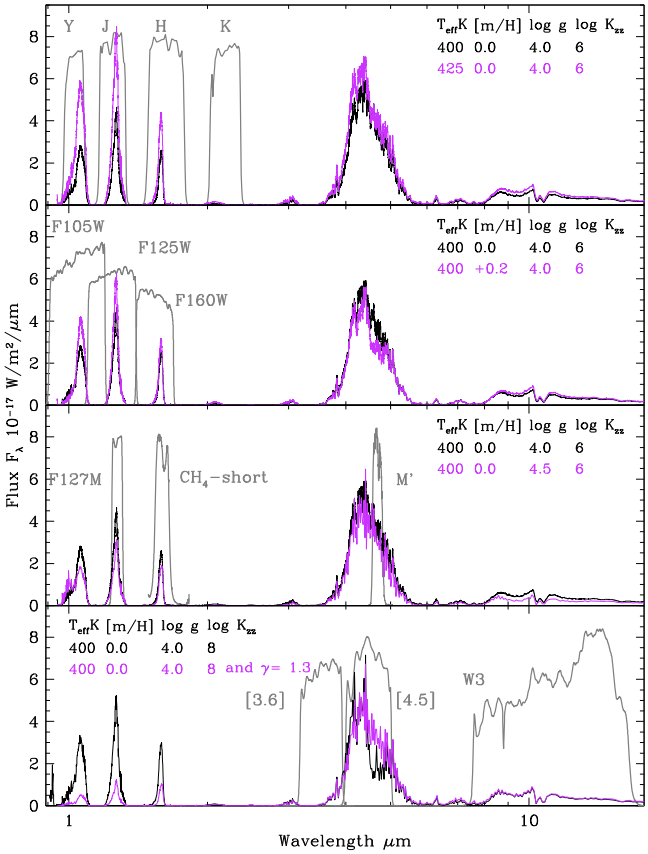

Figure 1. Spectral energy distributions of Y dwarfs with $T_{\rm eff} = 400$ K at a distance of 10 pc for $0.9 \leqslant \lambda\,(\mu{\rm m}) \leqslant 17.8$, generated by Tremblin et al. (2015) models. In the top panel, spectra are shown for different $T_{\rm eff}$, in the next panel [*m/H*] is varied, in the next $\log g$ is varied, and the bottom panel demonstrates the effect of changing the diffusion coefficient K_{zz} and the adiabatic index γ (see text). The MKO *YJHKM′* and CH_4; the *HST* WFC3 F105W, F125W, F127M, and F160W; the *WISE* W3; and the *Spitzer* [3.6] and [4.5] bandpasses are also shown.

The shape of the *Y*-band flux peak appears sensitive to gravity in Figure 1. Not shown in Figure 1 (but demonstrated later in the fits of synthetic to observed spectra) is that a decrease in metallicity has a similar effect. Leggett et al. (2015, their Figure 5) show that the 1 μm flux from a 400 K Y dwarf emerges between the H_2O and CH_4 absorption bands, in a region where NH_3 and pressure-induced H_2 opacity is important. H_2 opacity is sensitive to both gravity and metallicity (e.g., Liu et al. 2007), and the change in shape of the *Y*-band flux peak is likely due to changes in the H_2 opacity.

Figure 1 shows that much of the flux from a 400 K Y dwarf is emitted in the *Spitzer* [4.5] bandpass, which is similar to the *WISE* W2 bandpass. In fact, the T15 models show that, for $300 \leqslant T_{\rm eff}\,({\rm K}) \leqslant 500$ and $4.0 \leqslant \log g \leqslant 4.5$, 45%–54% of the total flux is emitted through this bandpass. The percentage of the total flux emitted at $\lambda < 2.5\,\mu$m decreases from 20% to <1% as $T_{\rm eff}$ decreases from 500 to 300 K, with the remaining 30%–50% emitted at $\lambda > 5\,\mu$m.

Because half the energy of Y dwarfs is emitted in the [4.5] bandpass, the value of [4.5] is an important constraint on bolometric luminosity and therefore $T_{\rm eff}$. Figure 2 shows $T_{\rm eff}$ as a function of $M_{[4.5]}$ in the left panel and $T_{\rm eff}$ as a function of $\log g$ in the right panel. The sequences in the left panel are from

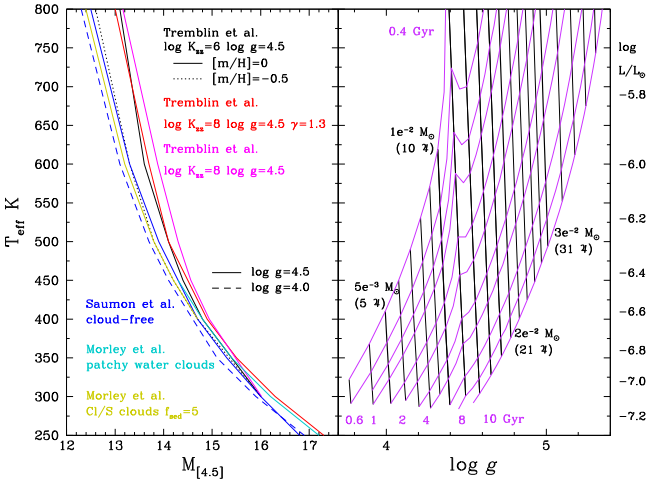

Figure 2. Effective temperature $T_{\rm eff}$ (K) is plotted on the y axis with absolute [4.5] magnitude on the x axis in the left panel and $\log g$ in the right panel. The right axis gives $\log L/L_{\odot}$ values. Sequences in the left panel are from various model atmospheres as indicated in the legend. Sequences in the right panel are taken from Saumon & Marley (2008) evolutionary models. In the right panel, violet lines are isochrones for ages as indicated along the bottom, and the almost vertical black sequences are lines of constant mass. From left to right, sequences for 0.003, 0.004, 0.005, 0.006, 0.007, 0.008, 0.009, 0.010, 0.012, 0.014, 0.016, 0.018, 0.020, 0.022, 0.024, 0.026, 0.028, 0.030, 0.035, 0.040, 0.045, and 0.050 solar mass are shown. One solar mass = 1047 Jupiter masses.

the various atmospheric models used in the work, which are described below. The sequences in the right panel are taken from the evolutionary models of Saumon & Marley (2008).

The cold Y dwarfs are intrinsically faint as they have a radius similar to that of Jupiter's. This low luminosity limits detection to nearby sources only, and all the known Y dwarfs with measured parallaxes are within 20 pc of the Sun (see Section 7). We assume therefore that the ages of the Y dwarfs should be typical of the solar neighborhood, and we limit the evolutionary sequences in Figure 2 to ages of 0.4–10 Gyr. For reference, the Galactic thin disk is estimated to have an age of 4.3 ± 2.6 Gyr (e.g., Bensby et al. 2005). The right panel of Figure 2 shows that for our sample we expect a range in $\log g$ of 3.8–4.8 and a range in mass of 3–23 Jupiter masses.

3. Model Atmospheres

In this work we use cloud-free model atmospheres from Saumon et al. (2012, hereafter S12) and T15. We also use models that include homogeneous layers of chloride and sulfide clouds from M12 and patchy water cloud models from M14. We do not use PHOENIX models, which have not been validated for $T_{\rm eff} < 400$ K,[6] or the Hubeny & Burrows (2007) models, which do not include the recent improvements to the CH_4, H_2, and NH_3 line lists.

Models for surface gravities given by $\log g = 4.0$, 4.5, and 4.8 were used, with a small number of $\log g = 3.8$ models for the lowest temperatures, as appropriate for this sample (see Figure 2). The T15 models include nonsolar metallicities of $[m/H] = -0.5$ and $[m/H] = +0.2$, and a few models were also generated with $[m/H] = -0.2$. This range in metallicities covers the expected range for stars in the Galactic thin disk (e.g., Bensby et al. 2005). The T15 models include an updated CH_4 line list (Yurchenko & Tennyson 2014), but they do not include opacities of PH_3 or rain-out processes for condensates, as do the S12, M12, and M14 models. For this work, a small number of T15 models with an adjusted adiabat were generated as described below.

The T15 models include nonequilibrium chemistry driven by vertical gas transport and parameterized with an eddy diffusion coefficient K_{zz} ($\rm cm^2\ s^{-1}$). The S12, M12, and M14 models are in chemical equilibrium. Vertical gas transport brings long-lived molecular species such as CO and N_2 up into the brown dwarf photosphere. Mixing occurs in the convective zones of the atmosphere and may occur in the nominally quiescent radiative zone via processes such as gravity waves (Freytag et al. 2010) or fingering instability (T15). If mixing occurs faster than local chemical reactions can return the species to local equilibrium, then abundances can be different by orders of magnitude from those expected for a gas in equilibrium (e.g., Noll et al. 1997; Saumon et al. 2000; Golimowski et al. 2004; Leggett et al. 2007; Visscher & Moses 2011; Zahnle & Marley 2014). The left panel of Figure 2 shows that, for a given $T_{\rm eff}$ and for $T_{\rm eff} \gtrsim 450$ K, the introduction of mixing increases $M_{[4.5]}$. This is due to the dredge-up of CO, which absorbs at 4.4–5.0 μm (e.g., M14, their Figure 7). For the coldest objects, the CO lies very deep in the atmosphere and is not expected to significantly impact the 4.5 μm flux. While CO absorption is enhanced by mixing, NH_3 absorption is diminished because of the dredge-up of N_2. In Figure 1 the black lines in the top and bottom panels are model spectra calculated for the same temperature, gravity, and metallicity, but with different values of K_{zz}. The increased mixing in the bottom panel results in stronger CO absorption at 4.5 μm and weaker NH_3 absorption in the near-infrared and at $\lambda \sim 10$ μm.

Various species condense in these cold atmospheres, forming cloud decks. For T dwarfs with $500 \lesssim T_{\rm eff}$ (K) $\lesssim 1300$, the condensates consist of chlorides and sulfides (e.g., Tsuji et al. 1996; Ackerman & Marley 2001; Helling et al. 2001; Burrows et al. 2003; Knapp et al. 2004; Saumon & Marley 2008; Stephens et al. 2009; Marley et al. 2012, M12, Radigan et al. 2012; Faherty et al. 2014). As $T_{\rm eff}$ decreases further, the next species to condense are calculated to be H_2O for $T_{\rm eff} \approx 350$ K and NH_3 for $T_{\rm eff} \approx 200$ K (Burrows et al. 2003, M14). A comparison of the cloudy and cloud-free sequences in Figure 2 shows that the clouds are not expected to affect the 4.5 μm flux until temperatures are low enough for water clouds to form. These water clouds are expected to scatter light in the near-infrared and absorb at $\lambda \gtrsim 3$ μm (e.g., M14, their Figure 2). For the warmer Y dwarfs with $T_{\rm eff} \approx 400$ K, the chloride and sulfide clouds lie deep in the atmosphere, but they may nevertheless affect light emitted in particularly clear opacity windows, such as the Y and J bands. Such clouds may be the cause of the (tentative) variability seen at Y and J for the Y0 WISEA J173835.52 +273258.8 (hereafter W1738), which also exhibits low-level variability at [4.5] (Leggett et al. 2016a).

Tremblin et al. (2016) show that brown dwarf atmospheres can be subject to thermochemical instabilities that could induce turbulent energy transport. This can change the temperature gradient in the atmosphere, which in turn can produce the observed brightening at J across the L- to T-type spectral boundary, without the need for cloud disruption (e.g., Marley et al. 2010). Tremblin et al. model the L-to-T transition by increasing the adiabatic index, which leads to warmer temperatures in the deep atmosphere and cooler temperatures in the upper regions. We have similarly experimented with

[6] http://perso.ens-lyon.fr/france.allard/

modified adiabats for this work, that is, using pressure–temperature profiles not described by adiabatic cooling of an ideal gas. For an ideal gas, adiabatic cooling is described by $P^{(1-\gamma)}T^{\gamma}$ = constant. Here, γ is the ratio of specific heats at constant pressure and volume. For hydrogen gas, $\gamma = 1.4$. Model spectra were generated with $\gamma = 1.2$, 1.3, and 1.35. We found that $\gamma = 1.35$ produced spectra indistinguishable from adiabatic cooling, and the observations presented later do not support a γ value as low as 1.2. Hence we only explore models with $\gamma = 1.3$ here.

Brown dwarf atmospheres are turbulent. It is likely that vertical mixing, cloud formation, thermal variations, and nonadiabatic energy transport are all important. Full three-dimensional hydrodynamic models are needed. In the meantime, we compare available models to new data we present in the next two sections. Although no model is perfect, we do find that the models that include vertical mixing can be used to estimate the properties of Y dwarfs.

4. New Gemini Observations

4.1. GNIRS Near-infrared Spectrum for WISEA J041022.75+150247.9

WISEA J041022.75+150247.9 (hereafter W0410) is a Y0 brown dwarf that was discovered in the *WISE* database by Cushing et al. (2011). Cushing et al. (2014) present a spectrum of W0410 that covers the wavelength range 1.07–1.70 μm at a resolution $R \approx 130$. The shape of the spectrum at 0.98–1.07 μm is sensitive to gravity and metallicity (Section 2), and for this reason we obtained a $0.95 \leqslant \lambda(\mu\mathrm{m}) \leqslant 2.5$ spectrum using GNIRS at Gemini North on 2016 December 24 and 25 via program GN-2016B-Q-46. GNIRS was used in cross-dispersed mode with the 32 l/mm grating, the short camera, and the 0.″675 slit, giving $R \approx 700$. A central wavelength of 1.65 μm resulted in wavelength coverage for orders 3–7 of 1.87–2.53 μm, 1.40–1.90 μm, 1.12–1.52 μm, 0.94–1.27 μm, and 0.80–1.08 μm. Flat-field and arc images were obtained using lamps on the telescope, and pinhole images were obtained to trace the location of the cross-dispersed spectra. A total of 18 frames with a 300 s exposure were obtained on W0410 on December 24 and 10 frames with a 300 s exposure on December 25. Both nights were clear, with seeing around 0.″8 on the first night and around 1.″0 on the second. GNIRS suffered from electronic noise on the second night, so we used the data from December 24 only. An "ABBA" offset pattern was used with offsets of 3″ along the slit. Bright stars were observed before and after W0410 on December 24 to remove telluric absorption features and produce an instrument response function; the F2V HD 19208 was observed before and the F3V HD 33140 was observed after. Template spectra for these spectral types were obtained from the spectral library of Rayner et al. (2009). The data were reduced in the standard way using routines supplied in the IRAF Gemini package. The final flux calibration of the W0410 spectrum was achieved using the observed *YJHK* photometry. Figure 3 shows the new spectrum and the lower resolution Cushing et al. (2014) spectrum for reference. We compare the spectrum to models in Section 9.

4.2. FLAMINGOS-2 Near-infrared Spectra for WISE J071322.55−291751.9 and WISEA J114156.67−332635.5

WISE J071322.55−291751.9 (hereafter W0713) is a Y0 brown dwarf that was discovered in the *WISE* database by Kirkpatrick et al. (2012). Kirkpatrick et al. present a spectrum

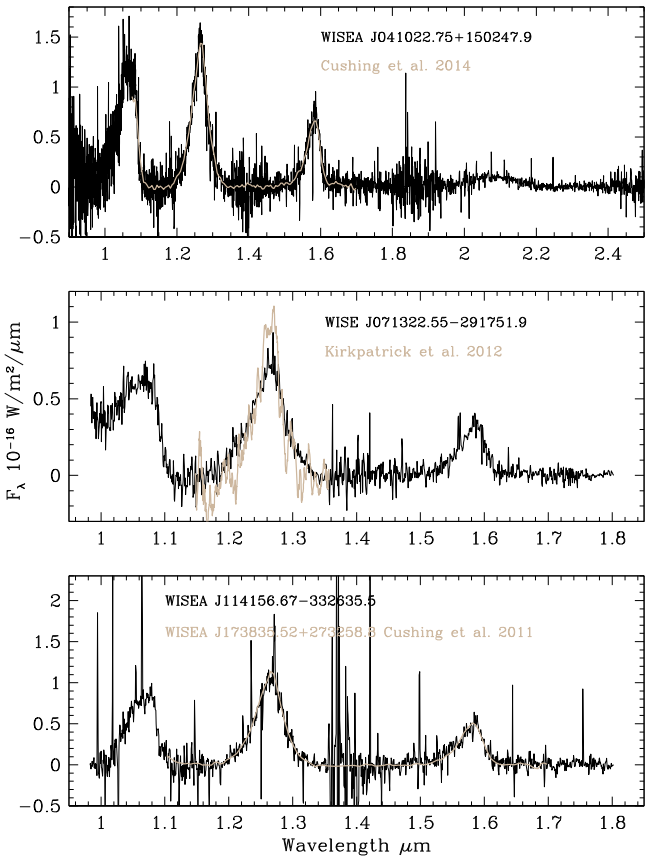

Figure 3. Black lines in the top, middle, and bottom panels are unsmoothed spectra of WISEA J041022.75+150247.9, WISE J071322.55−291751.9, and WISEA J114156.67−332635, respectively, determined here. Previously published spectra of the first two objects are shown as tan lines. In the bottom panel, the tan line is the spectrum of the Y0 standard WISEA J173835.52 +273258.8, which is very similar in shape to WISE 1141.

of W0713 that covers the *J* band only. WISEA J114156.67 −332635.5 (hereafter W1141) was discovered in the *WISE* database and was presented by Tinney et al. (2014). No near-infrared spectrum has been published for this object, but a type of Y0 was estimated by Tinney et al. based on absolute magnitudes and colors. We obtained near-infrared spectra for these two objects using FLAMINGOS-2 at Gemini South on 2017 February 3 and 7, via program GS-2017A-FT-2. The *JH* grism was used with the four-pixel (0.″72) slit, giving $R \approx 600$. The wavelength coverage was 0.98–1.80 μm. We compare the spectra to models in Section 9.

W1141 was observed on 2017 February 3 in thin cirrus with seeing 0.″8. An "ABBA" offset pattern was used with offsets of 10″ along the slit. A total of 18 frames with a 300 s exposure were obtained, as well as flat-field and arc images using lamps on the telescope. The F5V star HD 110285 was observed immediately following W1141. A template spectrum for F5V was obtained from the spectral library of Rayner et al. (2009). The bright star was used to remove telluric features and provide an instrument response function, and the final flux calibration was achieved using the *J* photometry given by Tinney et al. (2014). The data were reduced in the standard way using routines supplied in the IRAF Gemini package. Figure 3 shows our spectrum for this object, compared to the low-resolution Cushing et al. (2011) *JH* spectrum of W1738, which currently defines the Y0 spectral standard. The spectral shapes are almost

identical, and we confirm the Y0 spectral type estimated photometrically by Tinney et al. (2014).

W0713 was observed on 2017 February 7 in clear skies with seeing 0.″7. An "ABBA" offset pattern was used with offsets of 10″ along the slit. A total of 12,300 s frames were obtained, as well as flat-field and arc images using lamps on the telescope. The A3V star HD 43119 was observed immediately before W0713. A template spectrum for A3V was obtained from the Pickles (1998) spectral atlas. The bright star was used to remove telluric features and provide an instrument response function, and the final flux calibration was achieved using the *J* photometry given by Leggett et al. (2015). This was consistent with the more uncertain *Y* magnitude, but inconsistent with *H* by 5σ. Although variability cannot be excluded, the model fit shown later does a reasonable job of reproducing the entire spectrum, and we believe the discrepancy is due to the lower signal-to-noise ratio (S/N) in the *H* spectral region. Figure 3 shows our W0713 spectrum together with the Kirkpatrick et al. (2012) *J*-band spectrum of this object, which has been flux-calibrated by the *J* photometry. The Kirkpatrick et al. spectrum appears noisier, but it is consistent with our data.

4.3. NIRI Y, CH_4(short), and M′ for WISE J085510.83–071442.5

W0855 was discovered as a high proper motion object by Luhman (2014) in *WISE* images. W0855 is the intrinsically faintest and coolest object known outside the solar system at the time of writing, with effective temperature $T_{\rm eff} \approx 250$ K and $L/L_{\odot} \approx 5e-8$ (based on Stefan's law and radii given by evolutionary models). W0855 is 2.2 pc away and has a high proper motion of $-8.''10\,{\rm yr}^{-1}$ in R.A. and $+0.''70\,{\rm yr}^{-1}$ in decl. (Luhman & Esplin 2016, hereafter LE16).

We obtained photometry for W0855 on Gemini North using NIRI at *Y* and CH_4(short) via program GN-2016A-Q-50, and at *M*′ via program GN-2016A-FT-10. The photometry is on the MKO system, but there is some variation in the *Y*-filter bandpass between the cameras used on Maunakea, and $Y_{\rm NIRI} - Y_{\rm MKO} = 0.17 \pm 0.03$ magnitudes for late-type T and Y dwarfs (Liu et al. 2012). At the time of our observations (2015 December to 2016 March), the only published near-infrared detection of W0855 was a *J*-band measurement (Faherty et al. 2014). The *Y* and CH_4(short) observations were obtained in order to provide a near-infrared SED for this source. The *M*′ observation was obtained to probe the degree of mixing in the atmosphere, as described in Section 8.1.

All nights were photometric, and the seeing was 0.″5–0.″8. Photometric standards FS 14, FS 19, and FS 126 were used for the *Y* and CH_4(short) observations, and HD 77281 and LHS 292 were used for the *M*′ observations (Leggett et al. 2003, 2006; UKIRT online catalogs[7]). The photometric standard FS 20 with a type of DA3 was also observed in the CH_4(short) filter. This standard has $J - H = -0.03$ mag and $H - K = -0.05$ mag, that is, very close to a Vega energy distribution across the *H* bandpass. FS 20 confirmed that NIRI CH_4(short) zero points could be determined by adopting $CH_4 = H$ for all the standards observed, and we found the zero point to be 22.95 ± 0.03 mag. W0855 and the calibrators were offset slightly between exposures using a five- or nine-position telescope dither pattern. Atmospheric extinction corrections between W0855 and the nearby calibrators were not applied as these are much smaller than the measurement uncertainty (Leggett et al. 2003, 2006). The measurement uncertainties were estimated from the sky variance and the variation in the aperture corrections.

The *Y* and CH_4(short) data were obtained using the NIRI *f*/6 mode, with a pixel size of 0.″12 and a field of view (FOV) of 120″. Individual exposures were 120 s at *Y* and 60 s at CH_4(short). *Y* data were obtained at air masses ranging from 1.1 to 1.9 on 2016 February 16, 17, 18, and 23. CH_4(short) data were obtained at air masses ranging from 1.1 to 1.5 on 2015 December 25 and 26, 2016 January 19, February 1, and March 12 and 13. The total on-source integration time was 7.1 hr at *Y* and 14.7 hr at CH_4(short). Calibration lamps on the telescope were used for flat-fielding, and the data were reduced in the standard way using routines supplied in the IRAF Gemini package. Images from different nights were combined after shifting the coordinates to allow for the high proper motion of the target. The shift per day was −0.191 pixels in *x* and +0.017 pixels in *y*. Aperture photometry with annular skies was carried out, using an aperture diameter of 1.″2 and using point sources in the image to determine the aperture corrections.

The *M*′ data were obtained using the NIRI f/32 mode, with a pixel size of 0.″02 and a FOV of 22″; individual exposures were 24 s composed of 40 coadded 0.6 s frames. Data were obtained at an air mass of 1.1 to 1.4 on 2016 March 11. The total on-source integration time was 1.6 hr at *M*′. Flat fields were generated from sky images created by masking sources in the science data. Although the exposure time was short, the background signal through this 5 μm filter is high and can vary quickly. Because of this, after flat-fielding the data, we subtracted adjacent frames and then shifted the subtracted frames to align the calibrator or W0855 before combining the images. As the data were taken on one night, no correction had to be made for W0855's proper motion. Aperture photometry with annular skies was carried out using an aperture diameter of 0.″8. Aperture corrections were determined from the photometric standards.

W0855 was not detected in the *Y* filter, but it was detected in CH_4(short) and *M*′. Figure 4 shows two CH_4(short) images. One uses data taken in 2015 December and 2016 January, and the other uses data taken in 2016 March. The northwest motion of W0855 is apparent. Figure 4 also shows the stacked *M*′ and *Y* image. The measured magnitudes or detection limits are given in Table 1. Our measurement of $Y > 24.5$ mag is consistent with the Beamin et al. (2014) measurement of $Y > 24.4$ mag. Our measurement of CH_4(short) $= 23.38 \pm 0.20$ mag is consistent with the 23.2 ± 0.2 mag measured by LE16 and the 23.22 ± 0.35 mag determined by Zapatero Osorio et al. (2016) from analysis of the LE16 data.

4.4. NIRI M′ for CFBDS J005910.90−011401.3, 2MASSI J0415195−093506, UGPS J072227.51−054031.2, 2MASSI J0727182+171001, and WISEPC J205628.90+145953.3

The *M*′ data for a sample of T and Y dwarfs was obtained via program GN-2016B-Q-46 using NIRI on Gemini North in the same configuration as described in Section 4.3. The *M*′ observations were obtained to probe the degree of mixing in brown dwarf atmospheres, as described in Section 8.1. All nights were photometric with seeing varying night to night from 0.″4 to 1.″1. The data were reduced in the same way as the W0855 *M*′ data. The results are given in Table 1.

[7] http://www.ukirt.hawaii.edu/astronomy/calib/phot_cal/

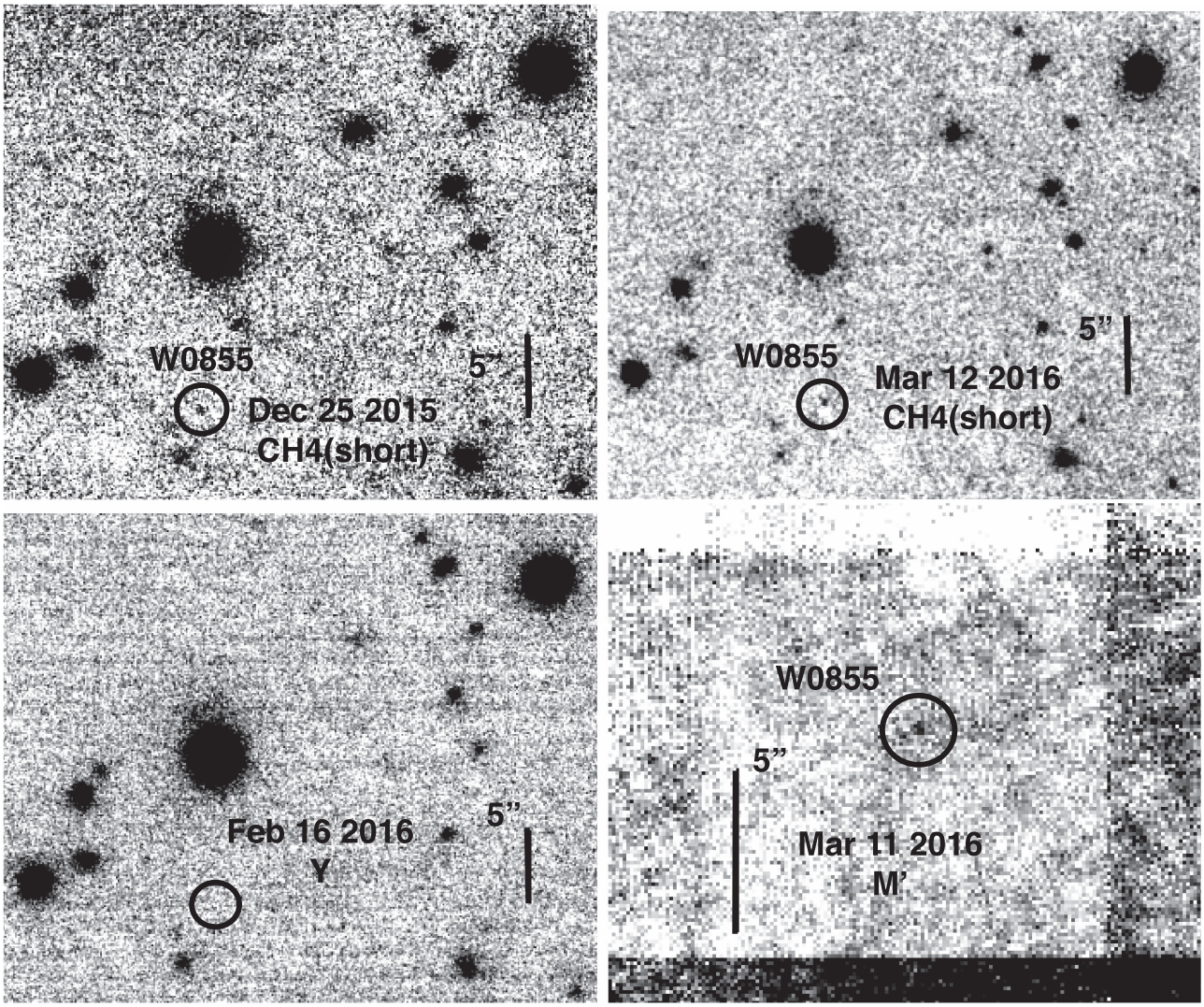

Figure 4. NIRI images of WISE J085510.83−071442.5. North is up and east to the left, and the scale is indicated by the 5″ vertical bar. The source is circled in the CH_4(short) and M' images. The source is not detected in Y; the circle indicates the expected location.

CFBDS J005910.90−011401.3 is a T8.5 dwarf discovered by Delorme et al. (2008). The T dwarf was observed on 2016 July 18 and 2016 October 11. The second data set was taken at a lower air mass, and we used the data from October 11 only. A total of 207 24 s dithered images were obtained for an on-source time of 1.4 hr. The air mass range was 1.07–1.26. Also observed on 2016 October 11 was UGPS J072227.51-054031.2, a T9 dwarf discovered by Lucas et al. (2010). Thirty-six 24 s dithered images were obtained for an on-source time of 14 minutes, at an air mass of 1.2. The photometric standards HD 1160, HD 22686, and HD 40335 were used as M' calibrators on 2016 October 11.

2MASSI J0415195−093506 is a T8 dwarf discovered by Burgasser et al. (2002). The T dwarf was observed on 2016 October 22. A total of 181 24 s dithered images were obtained for an on-source time of 1.2 hr. The air mass range was 1.18–1.30. The photometric standard HD 22686 was used for calibration.

2MASSI J0727182+171001 is a T7 dwarf discovered by Burgasser et al. (2002). The T dwarf was observed on 2017 January 9. A total of 153 24 s dithered images were obtained for an on-source time of 1.0 hr. The air mass range was 1.0–1.1. The photometric standards HD 40335 and HD 44612 were used for calibration.

WISEPC J205628.90+145953.3 (hereafter W2056) is a Y0 brown dwarf that was discovered in the *WISE* database by Cushing et al. (2011). W2056 was observed on 2016 July 13. A total of 244 24 s dithered images were obtained for an on-source time of 1.6 hr. The air mass range was 1.0–1.5. The photometric standards G 22-18 and HD 201941 were used as calibrators. The offsets were such that one corner of the stacked image contained the 2MASS star 20562847+1500092. This star has 2MASS magnitudes $J = 13.45 \pm 0.03$, $H = 13.18 \pm 0.04$, and $K_s = 13.20 \pm 0.03$ mag. We measure $M' = 13.21 \pm 0.15$ mag for this star. The near-infrared colors suggest a spectral type of G0 (Covey et al. 2007), and the measured $K_s - M' = -0.01 \pm 0.15$ mag is consistent with the color expected for the spectral type (e.g., Davenport et al. 2014).

4.5. Revised FLAMINGOS-2 H for WISEA J064723.24623235.4

We obtained H data for the Y1 WISEA J064723.24−623235.4 (Kirkpatrick et al. 2013, hereafter W0647) using

Table 1
New Gemini NIRI Photometry

Name	Spectral Type	Y[a] (err)	CH_4(short) (err)	H (err)	M' (err)
			magnitudes		
CFBDS J005910.90−011401.3	T8.5	…	…	…	13.68(0.15)
2MASSI J0415195−093506	T8	…	…	…	12.47(0.08)
WISEA J064723.24−623235.4	Y1	…	…	23.11(0.27)	…
UGPS J072227.51−054031.2	T9	…	…	…	12.11(0.06)
2MASSI J0727182+171001	T7	…	…	…	12.97(0.08)
WISE J085510.83−071442.5	>Y2	>24.5[b]	23.38(0.20)	…	13.95(0.20)
WISEPC J205628.90+145953.3	Y0	…	…	…	14.00(0.15)

Notes.
[a] The NIRI Y magnitudes have been put on the MKO Y system as described in the text.
[b] 3σ detection limit.

Table 2
New Near-infrared Photometry from WFC3 and HAWK-I Archives

Name(R.A.) (Decl.)	Spectral Type	F105W (err)	F125W (err)	F127M (err)	F160W (err)	J (err)	H (err)	WFC3 PI, ID HAWK-I PI, ID
				magnitudes				
WISEA J014807.34 −720258.7	T9.5	…	…	18.52 (0.02)	…	18.92 (0.02)	…	Biller 12873 Forveille 091.C-0543(D)
WISEA J032504.52 −504403.0	T8	…	…	…	…	18.90 (0.03)	…	Cushing 089.C-0042(A)
WISE J041358.14 −475039.3	T9	…	20.45 (0.11)	…	20.22 (0.12)	19.61 (0.02)	20.20 (0.03)	Cushing 12970, Gelino 12972 Cushing 089.C-0042(A)
UGPS J072227.51 −054031.2	T9	18.12 (0.03)	17.32 (0.03)	16.00 (0.03)	17.13 (0.03)	…	…	Liu 12504
WD 0806 −661B	Y1	25.97 (0.20)	25.92 (0.30)	24.80 (0.30)	25.46 (0.10)	…	…	Gelino 13428
WISEPC J104245.23 −384238.3	T8.5	…	…	18.37 (0.10)	19.33 (0.10)	18.74 (0.03)	19.21 (0.02)	Biller 12873, Gelino 12972 Cushing 089.C-0042(A)
ULAS J123828.51 +095351.3	T8	…	…	18.24 (0.11)	…	…	…	Burgasser 11666

FLAMINGOS-2 on Gemini South, which were presented in Leggett et al. (2015). Leggett et al. (2015) give a lower limit for H only. We have examined in more detail the reduced image at the location of the source (provided by the contemporaneous J detection) and obtained a 3.5σ measurement, which is given in Table 1.

5. Photometry from Image Archives

We searched various archives for late-type T and Y dwarf images in order to determine transformations between photometric systems and complement our data set. The archived images were downloaded in calibrated form, and we carried out aperture photometry using annular sky regions. Aperture corrections were derived using bright sources in the field of the target. This section gives the resulting, previously unpublished, photometry.

We have also updated our near-infrared photometry for the T8 dwarf ULAS J123828.51+095351.3 using data release 10 of the UKIRT Infrared Deep Sky Survey (UKIDSS), processed by the Cambridge Astronomy Survey Unit (CASU) and available via the WFCAM Science Archive WSA.[8] We added two late-type T dwarfs that have UKIDSS and *WISE* data and that were identified by Skrzypek et al. (2016): J232035.29 +144829.8 (T7) and J025409.58+022358.7 (T8).

5.1. HST WFC3

We used the *HST* Mikulski Archive for Space Telescopes (MAST) to search for Wide Field Camera 3 (WFC3) data for late-type T and Y dwarfs taken with the F105W, F125W, F127M, or F160W filters. These filters were selected as they more closely map onto the ground-based Y, J, and H bandpasses (Figure 1), compared to for example F110W and F140W, which have also been used for brown dwarf studies. The "drz" files were used, which have been processed through the `calwf3` pipeline and geometrically corrected using `AstroDrizzle`. The photometric zero points for each filter were taken from the WFC3 handbook.[9] Previously unpublished WFC3 photometry for five T dwarfs and one Y dwarf was obtained and is presented in Table 2.

5.2. ESO VLT HAWK-I

Images obtained with the European Southern Observatory's (ESO) High Acuity Wide-field K-band Imager (HAWK-I) are published as reduced data via the ESO science archive facility. The data were processed by CASU, which produced

[8] http://wsa.roe.ac.uk/

[9] http://www.stsci.edu/hst/wfc3/phot_zp_lbn

Table 3
New Mid-infrared Photometry from IRAC and *WISE* Archives

Name	Spectral Type	[3.6](err)	[4.5](err)	W1(err)	W3(err)	IRAC PI, ID
			magnitudes			
2MASS J00345157+0523050[a]	T6.5	14.07(0.03)	12.52(0.03)	⋯	⋯	Fazio 30179
CFBDS J005910.90−011401.3	T8.5	⋯	⋯	⋯	12.38(0.13)	
WISE J014656.66+423410.0AB	T9.5	⋯	⋯	⋯	13.4(0.2)	
WISEA J014807.34−720258.7	T9.5	16.58(0.02)	14.56(0.02)	⋯	⋯	Kirkpatrick 70062
WISE J030449.03−270508.3	Y0	17.71(0.03)	15.48(0.03)	⋯	⋯	Pinfield 10135
WISE J035934.06−540154.6	Y0	⋯	⋯	19.1(0.2)	14.0(0.2)	
WISE J085510.83−071442.5	>Y2	⋯	⋯	⋯	11.9(0.3)	
ULAS J090116.23−030635.0	T7.5	16.38(0.03)	14.50(0.03)	⋯	⋯	Kirkpatrick 80109
WISEA J114156.67−332635.5	Y0	16.64(0.08)	14.66(0.03)	⋯	⋯	Kirkpatrick 80109
ULAS J150457.66+053800.8	T6.5	15.13(0.03)	14.08(0.03)	⋯	⋯	Kirkpatrick 80109
WISEPA J154151.66−225025.2	Y0.5	⋯	⋯	⋯	12.2(0.3)	
WISEA J163940.84−684739.4	Y0pec	16.23(0.03)	13.57(0.03)	⋯	⋯	Kirkpatrick 80109
WISEPA J182831.08+265037.8	>Y1	⋯	⋯	17.34(0.26)	⋯	
WISEA J205628.88+145953.6	Y0	16.06(0.10)	⋯	⋯	⋯	Dupuy 80233, Cushing 90015

Note.
[a] For 2MASS J00345157+0523050, we also measured [5.8] = 13.13 ± 0.03 and [8.0] = 12.41 ± 0.03 mag.

astrometrically and photometrically calibrated stacked and tiled images. The integration time was obtained from the "DIT" and "NDIT" entries in the FITS headers. Previously unpublished *J* and *H* photometry on the MKO system was obtained for four T dwarfs and is presented in Table 2.

5.3. Spitzer

The NASA/IPAC Infrared Science Archive (IRSA) was used to search the mid-infrared *Spitzer* [3.6], [4.5], [5.8], and [8.0] IRAC images. The postbasic calibrated data (PBCD) were downloaded and photometry obtained using the Vega fluxes given in the IRAC instrument handbook.[10] Previously unpublished IRAC photometry for four T dwarfs, two confirmed Y dwarfs, and one unconfirmed Y dwarf is presented in Table 3. We also re-extracted [3.6] photometry for W2056 from six images taken in 2012–2014, in order to more accurately remove artifacts caused by a nearby bright star. This result is also given in Table 3.

5.4. WISE

IRSA was used to examine the ALLWISE calibrated images taken in the W1 (3.4 μm) and W3 (12 μm) filters where the photometry was not listed in the *WISE* catalog. Zero points were provided in the data FITS headers. Previously unpublished W1 photometry is given for two Y dwarfs, and W3 for two T and three Y dwarfs, in Table 3.

In the process of examining the *WISE* image data for the known Y dwarfs, we also determined that the W1 photometry for the Y dwarf WISE J154151.65−225024.9 was compromised by nearby sources, and this measurement was removed from our photometric database.

6. Synthesized Photometry and Transformations between *HST* F1.05W, F1.25W, F1.27M, F1.60W; CH_4(short); and MKO *Y*, *J*, *H*

Schneider et al. (2015) present observed WFC3 F105W or F125W photometry for five late-T and 11 Y dwarfs. Beichman et al. (2014) present F105W and F125W photometry for an additional Y dwarf. Schneider et al. also present grism spectroscopy from which they calculate synthetic F105W and F125W photometry. In order to transform *HST* photometry and our CH_4 photometry onto the MKO system, we calculated the following colors (or a subset) from available near-infrared spectra: $Y-$F1.05W, $J-$F1.25W, $J-$F1.27M, $H-$F1.60W, and $H-CH_4$(short). Table 4 lists these newly synthesized colors for five T dwarfs and six Y dwarfs, using spectra from this work, Kirkpatrick et al. (2012), Knapp et al. (2004), Leggett et al. (2014, 2016b), Lucas et al. (2010), Schneider et al. (2015), and Warren et al. (2007).

Table 4 also gives synthetic MKO system colors for three T dwarfs and two Y dwarfs using spectra from this work, Kirkpatrick et al. (2011), and Pinfield et al. (2012, 2014). These five objects were selected as additions to our data set because they are either very late type or have been classified as peculiar and so potentially sample unusual regions of color–color space.

We have used the synthesized colors and measured MKO and *HST* photometry, where they both exist, to determine a set of transformations between the two systems as a function of type, for late-T and Y dwarfs. The photometry is taken from Leggett et al. (2015) and references therein, Schneider et al. (2015) and references therein, and this work. We have included colors from T15 spectra for $T_{\rm eff}$ = 400, 300, 250, and 200 K, with $\log g = 4.5$ and $\log K_{zz} = 6$, to constrain the transformations at very late spectral types. For the purposes of the fit, we adopt spectral types of Y0.5, Y1.5, Y2, and Y2.5 for the colors generated by models with $T_{\rm eff}$ = 400, 300, 250, and 200 K, respectively. We explored the sensitivity of the synthetic colors to the atmospheric parameters using $T_{\rm eff}$ = 300 K models with $\log g = 4.0$ and 4.5, $[m/H] = 0.0$ and −0.5, and $\log K_{zz} = 6$ and 8. We found a dispersion in $Y-$F1.05W, $J-$F1.25W, $J-$F1.27M, $H-$F1.60W, and $H-CH_4$(short) of 0.01–0.09 mag. We adopt a ±0.1 mag uncertainty in these model colors.

We performed weighted least-squares quadratic fits to the data. Figure 5 shows the data and the fits, and Table 5 gives the fit parameters for the transformations. Based on the scatter seen in Figure 5, we estimate the uncertainty in the transformations for the Y dwarfs to be ±0.10 mag. We have used the relationships given in Table 5 to estimate *Y*, *J*, and *H* magnitudes

[10] http://irsa.ipac.caltech.edu/data/SPITZER/docs/irac/iracinstrumenthandbook/17/

Table 4
Synthesized Near-infrared Colors from Spectra

Name	Spectral Type	$J-$F127M (err)	$H-$F160W (err)	$H-CH_4$ (err)	$Y-J$ (err)	$J-H$ (err)	$J-K$
				magnitudes			
ULAS J003402.77−005206.7[a]	T8.5	0.62(0.03)	−0.23(0.03)	0.60(0.03)	…	…	…
WISEA J014807.34−720258.7	T9.5	…	…	…	0.76(0.05)	−0.42(0.03)	−0.76(0.10)
WISE J030449.03−270508.3	Y0	…	…	…	0.53(0.15)	…	…
WISEA J033515.07+431044.7	T9	…	…	0.67(0.05)	…	…	…
WISEA J035000.31−565830.5	Y1	0.88(0.10)	…	…	…	…	…
WISEA J041022.75+150247.9	Y0	0.74(0.10)	−0.09(0.10)	0.83(0.10)	…	…	…
2MASSI J0415195−093506	T8	0.57(0.03)	−0.19(0.03)	0.58(0.03)	…	…	…
UGPS J072227.51−054031.2	T9	0.65(0.03)	−0.16(0.03)	0.67(0.03)	…	…	…
WISEA J114156.67−332635.5	Y0	…	…	…	0.57(0.03)	−0.39(0.05)	…
WISEPC J121756.91+162640.2A	T9	0.59(0.03)	−0.20(0.03)	0.61(0.03)	…	…	…
WISEPC J121756.91+162640.2B	Y0	0.75(0.03)	−0.14(0.03)	0.83(0.03)	…	…	…
WISEP J142320.86+011638.1[b]	T8pec	…	…	…	…	−0.41(0.06)	−1.48(0.15)
WISE J154151.65−225024.9	Y0.5	0.92(0.20)	−0.07(0.20)	…	…	…	…
WISEA J173835.52+273258.8	Y0	0.75(0.03)	−0.14(0.03)	0.83(0.03)	…	…	…
WISEA J205628.88+145953.6	Y0	0.72(0.05)	−0.22(0.05)	0.78(0.05)	…	…	…
WISEA J232519.55−410535.1[c]	T9pec	…	…	…	0.57(0.10)	−0.25(0.06)	−1.35(0.30)

Notes.
[a] For ULAS J003402.77−005206.7, we also synthesized $Y-$F105W $= -0.59 \pm 0.03$ and $J-$F125W $= -0.61 \pm 0.03$ mag.
[b] WISEP J142320.86+011638.1 is also known as BD +01°2920B (Pinfield et al. 2012).
[c] For WISEA J232519.55−410535.1 Data Release 4 of the VISTA VHS survey, McMahon et al. 2013 gives $J = 19.53 \pm 0.08$.

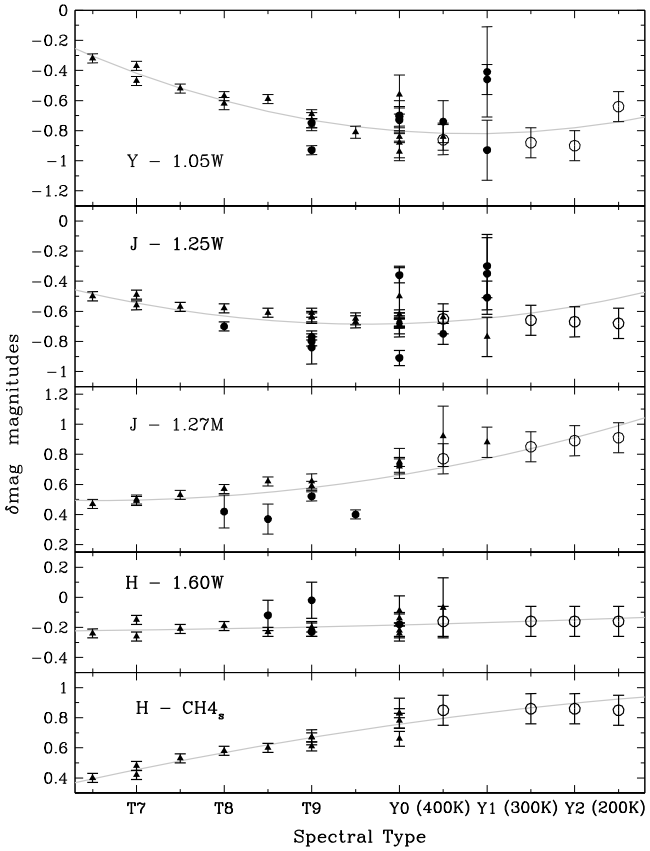

Figure 5. *HST*, CH_4(short), and MKO near-infrared colors as a function of spectral type. WISEPA J182831.08+265037.8 has been assigned a type of Y1. Solid circles are measured values, and triangles are synthesized from spectra. Open circles are calculated from Tremblin et al. (2015) models with $\log g = 4.5$ and $\log K_{zz} = 6.0$. The model effective temperature is given along the x axis, and we adopt 400 K = Y0.5, 300 K = Y1.5, 250 K = Y2, and 200 K = Y2.5. The parameters of the weighted quadratic fits are given in Table 5.

Table 5
Transformations between *HST*, CH_4(short), and MKO Near-infrared Colors

Color	$a0$	$a1$	$a2$
$Y-$F105W	2.42719	−0.601128	0.027812
$J-$F125W	1.228187	−0.398120	0.020710
$J-$F127M	1.092170	−0.1183161	0.014005
$H-$F160W	−0.21659	−0.008060	0.001134
$H-CH_4$	−0.679045	0.204865	−0.006130

Note. The transformation is applied as $color = a0 + (a1 \times Type) + (a2 \times Type^2)$, where *Type* runs from 7.5 to 12, corresponding to spectral types T7.5 to Y2. The estimated uncertainty in color is 0.10 mag (see text and Figure 5).

(or a subset) on the MKO system for seven Y dwarfs with *HST* and CH_4(short) photometry. The results are given in Table 6. We have expanded wavelength coverage for five of these Y dwarfs by adopting the synthetic colors derived by Schneider et al. (2015) from their spectra. These values are also given in Table 6. Table 6 also gives MKO photometry for W1141, determined using the synthesized colors given in Table 4.

WD0806−661B and W0855 have estimates of J, and J and H, respectively, determined in two ways (Table 6). The two values of J agree within the quoted uncertainties for both Y dwarfs (although only marginally so for W0855). The two values of H for W0855 differ by 1.8σ. We use a weighted average of the two measurements in later analysis, and we estimate the uncertainty in the average to be the larger of the uncertainty in the mean or one-half the difference between the two values.

7. New Astrometry and the Luminosity of WISE J014656.66+423410.0AB

LE16 refined the parallax and proper motion for W0855 using astrometry measured with multiepoch images from *Spitzer* and

Table 6
New Estimated MKO System *Y*, *J*, *H* Photometry for Y Dwarfs

Name	Spectral Type	*Y* (F105W) (err)	*Y*(*YJ*) (spectrum) (err)	*J* (F125W) (err)	*J* (F127M) (err)	*J*(*YJH*) (spectrum) (err)	*H* (F160W) (err)	*H* (CH_4) (err)	*H*(*JH*) (spectrum)
					magnitudes				
WD 0806 −661B	Y1	25.14[a] (22)	…	25.27[b] (32)	25.57[b] (32)	…	25.29 (14)	…	…
WISEA J082507.37[c] +280548.2	Y0.5	22.66 (11)	…	22.53 (10)	…	…	…	…	23.09 (18)
WISE J085510.83 −071442.5	>Y2[d]	26.54[e] (21)	…	25.84[f] (29)	25.37[f] (13)	…	23.71 (10)	24.19[g] (17)	…
WISEA J114156.67[h] −332635.5	Y0	…	20.33 (14)	…	…	…	…	…	20.15 (15)
WISEA J120604.25[c] +840110.5	Y0	20.89 (10)	…	20.38 (10)	…	…	…	…	20.97 (12)
WISEA J163940.84[c] −684739.4	Y0	20.54 (10)	…	20.47 (10)	…	…	…	…	20.59 (11)
WISEA J220905.75[c] +271143.6	Y0	23.04 (12)	…	…	…	22.94 (19)	…	…	22.48 (21)
WISEA J235402.79[c] +024014.1	Y1	…	…	22.72 (13)	…	…	…	…	22.53 (38)

Notes. Photometric error is in centimag.
[a] Consistent with Luhman et al. (2014) $Y > 23.2$ mag.
[b] Previous estimate $J = 25.00 \pm 0.10$ mag from F110W = 25.70 ± 0.08 mag (Luhman et al. 2014). The transformation between *HST* and MKO colors is better determined here, and we adopt the weighted average of *J*(F125W) and *J*(F127M) (Table 8).
[c] Photometry is based on Schneider et al. (2015) measurements of *HST* magnitudes and their synthetic colors from *HST* spectra.
[d] A spectral type of Y2 is used for the estimation of MKO photometry from the *HST* and CH_4 photometry.
[e] Consistent with our measurement of $Y > 24.5$ mag, and also Beamin et al. (2014) $Y > 24.4$ mag.
[f] Consistent with the faint limit of Faherty et al. (2014) $J = 25.0^{+0.53}_{-0.35}$ mag. We adopt the weighted average of *J*(F125W) and *J*(F127M) (Table 8).
[g] Based on the average of CH_4(short) = 23.38 ± 0.20 mag (this work) and CH_4(short) = 23.2 ± 0.2 mag (Luhman & Esplin 2016). We adopt the weighted average of *H*(F160W) and *H*(CH_4) (Table 8).
[h] Photometry is based on the *J* measurement given in Tinney et al. (2014) and the synthetic colors measured here (Table 4).

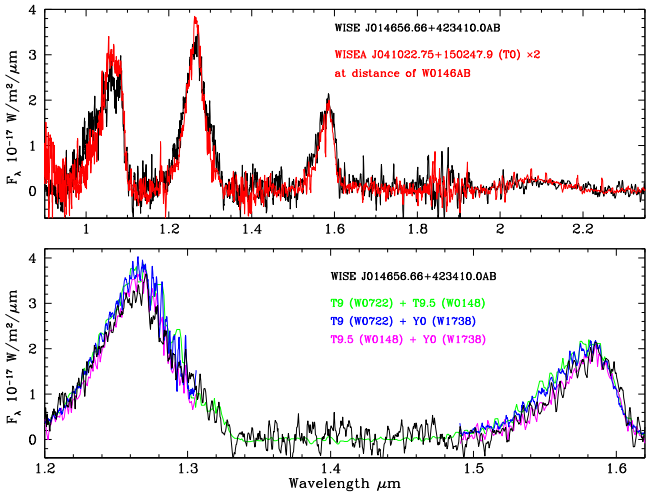

Figure 6. Observed spectrum of WISE J014656.66+423410.0AB (black line; Dupuy et al. 2015) is compared to composite spectra of very late T and early Y dwarfs. In the upper panel, the intrinsic *J*-band brightness of the template spectra is retained. In the lower panel, the *J*-band brightness is not retained, but the spectra that form the composite are scaled so that δJ equals that of the components of the W0146 binary (Dupuy et al. 2015). The upper panel demonstrates that the near-infrared combined-light spectrum of the binary is similar to that of a pair of Y0 dwarfs. The lower panel shows that the binary is likely composed of a T9.5 primary and a Y0 secondary. We adopt a spectral type of T9.5 for W0146AB and W0146A, and a type of Y0 for W0146B.

HST. They also presented new parallaxes for three Y dwarfs whose previous measurements had large uncertainties: WISE J035000.32−565830.2 (hereafter W0350), WISE J082507.35 +280548.5 (hereafter W0825), and WISE J120604.38 +840110.6 (hereafter W1206). Those measurements were based on the *Spitzer* IRAC images of these objects that were publicly available and the distortion corrections for IRAC from Esplin & Luhman (2016). We have measured new proper motions and parallaxes in the same way for three additional Y dwarfs whose published measurements are uncertain: WISE J053516.80 −750024.9 (hereafter W0535), WISEPC J121756.91 +162640.2AB (hereafter W1217AB), and WISEPC J140518.40 +553421.5 (hereafter W1405). We have also determined an improved parallax for WISE J014656.66+423410.0AB (hereafter W0146AB), which was classified as a Y0 in the discovery paper (Kirkpatrick et al. 2012) and reclassified as a T9 when it was resolved into a binary with components of T9 and Y0 (Dupuy et al. 2015).

In Table 7, we have compiled the parallaxes for W0350, W0825, and W1206 from LE16, the proper motions for those objects that were derived by LE16 but were not presented, and our new parallaxes and proper motions for W0146AB, W0535, W1217AB, and W1405. The uncertainties in the new parallax measurements are significantly smaller than those of the previously published values: 5–12 mas compared to 14–80 mas. The measurements for W1217AB and W1405 are consistent with previous measurements by Dupuy & Kraus (2013), Marsh et al. (2013), and Tinney et al. (2014). The measurement for W0535 differs from the previous measurement by Marsh et al. by 2σ. The measurement for W0146AB differs from the previous measurement by Beichman et al. (2014) by 3σ. In the appendix, Tables 11–14 give the

Table 7
New Astrometry

Name	Parallax ″ (err)	$\mu_\alpha \cos\delta$ ″ yr^{-1}(err)	μ_δ ″ yr^{-1}(err)
WISE J014656.66+423410.0AB[a]	0.054(0.005)	−0.455(0.004)	−0.024(0.004)
WISEA J035000.31−565830.5[b]	0.184(0.010)	−0.206(0.007)	−0.578(0.008)
WISE J053516.80−750024.9[c]	0.070(0.005)	−0.127(0.004)	0.013(0.004)
WISEA J082507.37+280548.2[b]	0.158(0.007)	−0.066(0.008)	−0.247(0.010)
WISEA J120604.25+840110.5[b]	0.085(0.007)	−0.585(0.004)	−0.253(0.005)
WISEPC J121756.91+162640.2AB[d]	0.113(0.012)	0.760(0.011)	−1.278(0.010)
WISEPC J140518.40+553421.5[e]	0.155(0.006)	−2.334(0.005)	0.232(0.005)

Notes.
[a] Astrometric measurements are given in Table 11.
[b] Parallax from Luhman & Esplin (2016).
[c] Astrometric measurements are given in Table 12.
[d] Astrometric measurements are given in Table 13.
[e] Astrometric measurements are given in Table 14.

astrometric measurements for W0146AB, W0535, W1217AB, and W1405.

We show in the next section that the revised parallax for W0146AB places the binary, and its components, in a region of the color–magnitude diagrams that is occupied by other T9/Y0 dwarfs. The previous parallax measurement implied an absolute magnitude 1.2 mag fainter, suggesting an unusually low luminosity (Dupuy et al. 2015). The upper panel of Figure 6 shows that the combined-light spectrum is very similar to what would be produced by a pair of Y0 dwarfs; that is, the system is not unusual. We have deconvolved the spectrum using near-infrared spectra of late-T and early-Y dwarfs as templates (a larger number of spectra are available than when Dupuy et al. deconvolved the spectrum). The absolute brightness of each input spectrum has been ignored, but the relative brightness of each input pair has been made to match the δJ magnitudes measured for the resolved system. The lower panel of Figure 6 shows that the T9 + T9.5 and T9 + Y0 composite spectra have slightly broader J and H flux peaks than observed for W0146AB, while a T9.5 primary with a Y0 secondary reproduces the spectrum quite well. We adopt a spectral type of T9.5 for W0146AB and W0146A, and a type of Y0 for W0146B.

8. Photometry: The Sample and Comparison to Models

Table 8 compiles the following observational data for the currently known sample of 24 Y dwarfs: parallax (in the form of a distance modulus); MKO System *YJHK*; *Spitzer* [3.6] and [4.5]; and *WISE* W1, W2, and W3 magnitudes. The data sources are given in the table. In the appendix, Table 15 gives an online data table with these values for the larger sample of late-T and Y dwarfs used in this work. We have compared these data to calculations by the models described in Section 3 via a large number of color–color and color–magnitude plots.

8.1. Constraining the Eddy Diffusion Coefficient K_{zz}

The M' observations allow a direct measurement of the strength of the CO absorption at 4.7 μm, as shown in Figure 1. Figure 7 shows [4.5]−M' as a function of $M_{[4.5]}$. The reduction in M' flux for the T dwarfs is evident in the figure. The CO absorption does not appear to be a strong function of gravity, as indicated by the similarity between the T15 $\log g = 4.0$ and

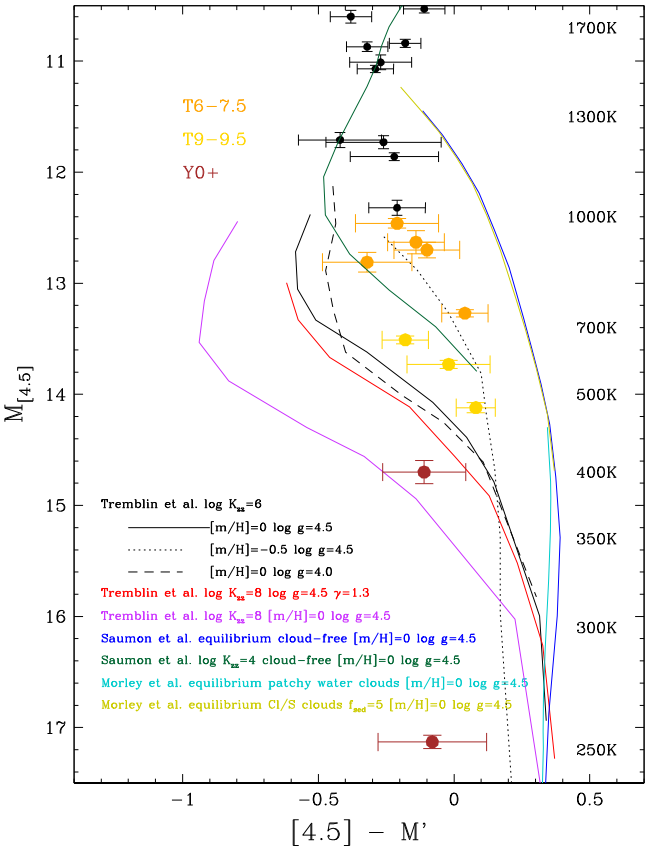

Figure 7. Absolute [4.5] as a function of the color [4.5]−M'. Solid circles are observational data, with colors indicating late-type T and Y dwarfs, as shown by the legend. Sequences are calculated by the models described in the legend (see also Section 3). Model $T_{\rm eff}$ values corresponding to $M_{[4.5]}$ are shown along the right axis. Absorption by CO at 4.7 μm, caused by vertical transport of gas, increases M'.

$\log g = 4.5$ sequences. The absorption does appear to be a function of metallicity and of the adiabat used for heat transport (see Section 3, and note the $\gamma = 1.3$ sequence in Figure 7 has $\log K_{zz} = 8$). We make the assumption that the majority of the dwarfs shown in Figure 7 do not have metallicities as low as −0.5 dex, and we show below that while the ad hoc change to the adiabat improves the model fits at some wavelengths, it is not preferred over the models with standard adiabatic

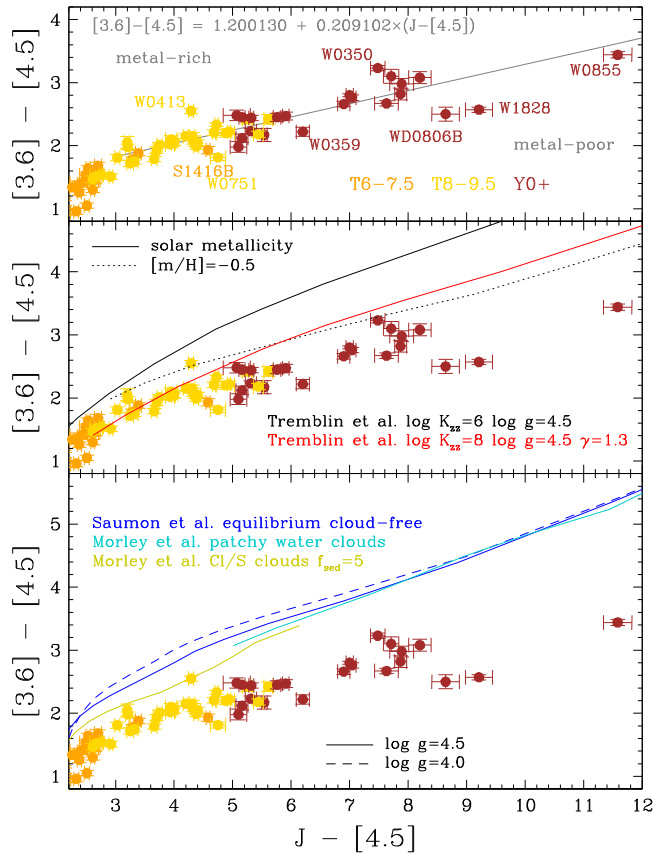

Figure 8. Color [3.6]−[4.5] as a function of J−[4.5]. Solid circles are observational data, with colors indicating spectral type as given in the legend. Outliers are identified by name in the top panel. In the top panel, the gray line is a linear fit to data with $J-[4.5]>3$ magnitudes, excluding sources that deviate by $>2\sigma$. The middle panel explores changing metallicity and the adiabatic gradient via T15 models, and the bottom panel explores the impact of gravity and clouds via S12, M12, and M14 models (see legends).

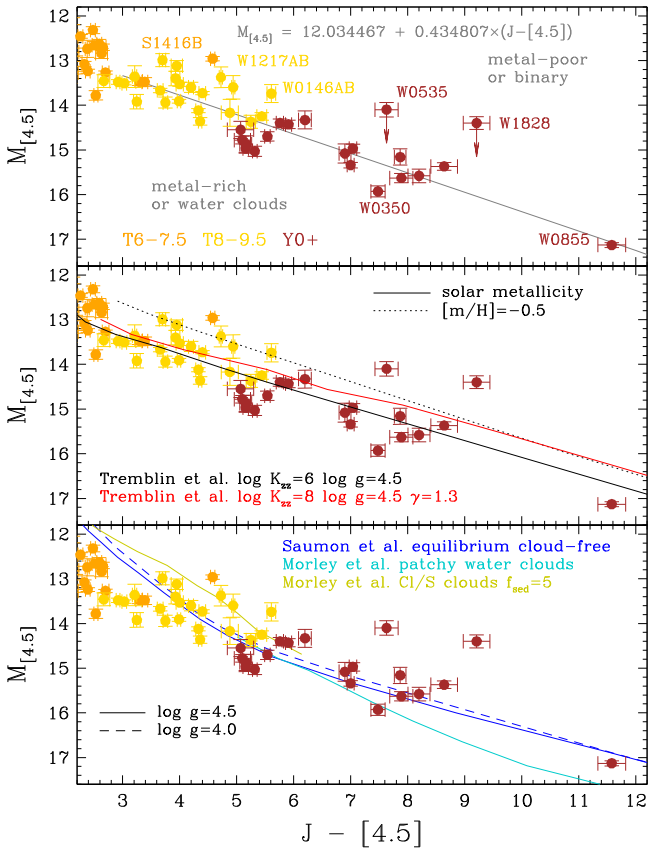

Figure 9. Absolute [4.5] as a function of the color $J-[4.5]$. Symbols and lines are as in Figure 8. W0535 and W1828 appear to be multiple sources, and the downward arrows indicate their location if the sources are a pair of identical Y dwarfs. Note that, for brown dwarfs, lines of constant gravity are close to iso-mass sequences (Figure 2, right panel). For Y dwarfs, $M_{[4.5]}$ correlates with $T_{\rm eff}$, and for a given $M_{[4.5]}$, lower gravity implies a lower mass and younger brown dwarf, and vice versa (Figure 2).

cooling. With those assumptions, Figure 7 indicates that $4 \lesssim \log K_{zz} \lesssim 6$ for mid-T to early-Y type brown dwarfs. This is consistent with previous model fits to T6–T8 brown dwarfs, where the fits were well constrained by mid-infrared spectroscopy (Saumon et al. 2006, 2007; Geballe et al. 2009). For the latest-T and early-Y dwarfs, we adopt $\log K_{zz}=6$. Figure 7 suggests that the coolest object currently known, W0855, may have a larger diffusion coefficient, and we explore this further in Section 10.5.

8.2. Metallicity and Multiplicity

The color–color plot best populated by the sample of Y dwarfs is $J-[4.5]$:$[3.6]-[4.5]$. This plot is shown in Figure 8. Figure 9 shows the color–magnitude plot $J-[4.5]$:$M_{[4.5]}$. The plots are divided into three panels. The top panel is data only, with a linear fit to sources with $J-[4.5]>3.0$ magnitudes, excluding sources that deviated by $>2\sigma$ from the fit. The average deviation from the linear fit along the y axes is 0.09 and 0.14 mag in Figures 8 and 9, respectively. The fit parameters are given in the figures. The middle panel of each figure compares the data to nonequilibrium T15 models that differ in metallicity and adiabat gradient. The bottom panel compares the data to S12, M12, and M14 equilibrium models, which differ in gravity and cloud cover.

Figures 8 and 9 show that none of the models reproduce the observed $[3.6]-[4.5]$ color. The cloud-free nonequilibrium models are better than the cloud-free equilibrium models for the T dwarfs, which are more impacted by the dredge-up of CO than the Y dwarfs (Figure 7). The reduction in the adiabatic index and the introduction of clouds improves the fit for the T dwarfs because in both cases the $\lambda\sim1$ μm light emerges from cooler regions of the atmosphere than in the adiabatic or cloud-free case (Morley et al. 2012 their Figure 5, Tremblin et al. 2016 their Figure 5). In the $J-[4.5]$:$M_{[4.5]}$ plot (Figure 9), however, the chemical equilibrium chloride and sulfide cloud model does not reproduce the observations of the T dwarfs, and the modified adiabat model does not reproduce the observations as well as the adiabatic model does. If we assume that the model trends in the colors with gravity, cloud, and metallicity are nevertheless correct, we can extract important information from Figures 8 and 9 for the Y dwarfs.

Figure 8 suggests that the $J-[4.5]$:$[3.6]-[4.5]$ colors of Y dwarfs are insensitive to gravity and clouds, but are sensitive to metallicity. The model trends imply that the following objects are metal-rich: W0350 (Y1) and WISE J041358.14−475039.3 (W0413, T9). Similarly, the following are metal-poor: WISEPA J075108.79−763449.6 (W0751, T9), WISE J035934.06−540154.6 (W0359, Y0), WD0806−661B (Y1), and W1828 (>Y1).

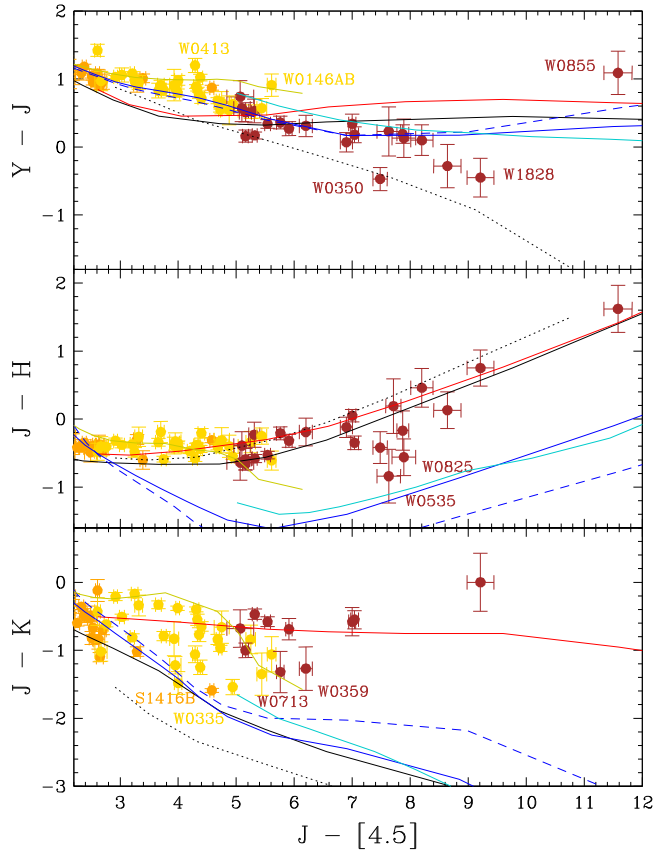

Figure 10. Near-infrared colors as a function of $J-[4.5]$. Symbols and lines are as in Figure 8.

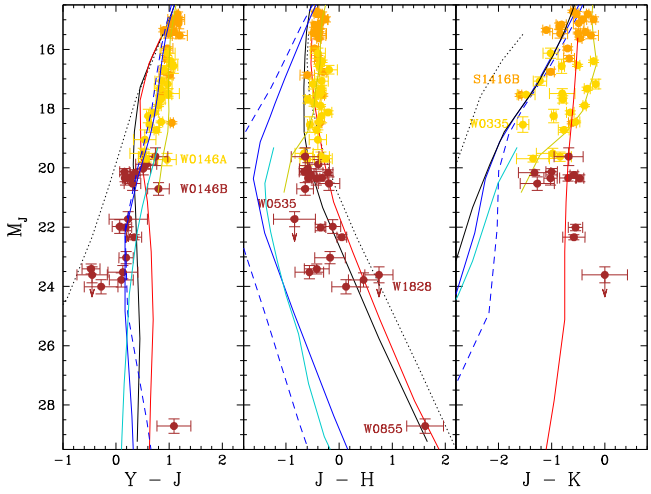

Figure 11. Absolute J magnitude as a function of near-infrared colors. Symbols and lines are as in Figure 8. W0535 and W1828 appear to be multiple sources, and the downward arrows indicate their location if the sources are a pair of identical Y dwarfs.

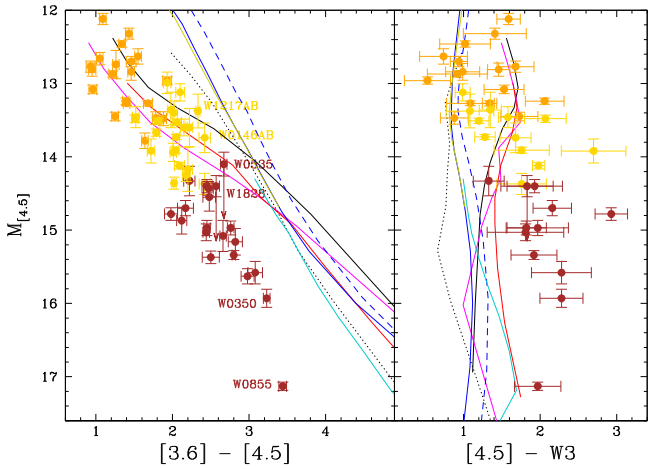

Figure 12. Absolute [4.5] as a function of mid-infrared colors. Symbols and lines are as in Figure 8. W0535 and W1828 appear to be multiple sources, and the downward arrows indicate their location if the sources are a pair of identical Y dwarfs.

Figure 9 suggests that $J-[4.5]$:$M_{[4.5]}$ is insensitive to gravity, but is sensitive to clouds and metallicity. Figure 9 supports a subsolar metallicity for W0359 and W1828 and a supersolar metallicity for W0350. Note that SDSS J1416 +1348B (S1416B, T7.5) is a known metal-poor and high-gravity T dwarf (e.g., Burgasser et al. 2010). The Y dwarfs, including W0855 in this plot, appear to be essentially cloud-free.

In any color–magnitude plot, multiplicity leads to over-luminosity. The Y dwarf sample size is now large enough, and the data precise enough, that we can identify W0535 and W1828 as likely multiple objects. We examined the drizzled WFC3 images of these two Y dwarfs for signs of elongation or ellipticity. Images of W0535 taken in 2013 September and December show no significant elongation or ellipticity, implying that if this is a binary system, then the separation is <3 au. A tighter limit was found by Opitz et al. (2016), who used Gemini Observatory's multiconjugate adaptive optics system to determine that any similarly bright companion must be within $\sim$1 au. For W1828, five WFC3 images taken in 2013 April, May, June, and August show marginal elongation and ellipticity of $16\pm8\%$. For this (nearer) source, the putative binary separation is $\lesssim$2 au.

8.3. Further Down-selection of Models

Figures 10 and 11 show near-infrared colors as a function of $J-[4.5]$ and absolute J as a function of near-infrared colors. In both figures, the T15 nonequilibrium models reproduce the trends in $Y-J$ and $J-H$ quite well. The S12, M12, and M14 equilibrium models reproduce $Y-J$ but do poorly with $J-H$, except for the chloride and sulfide models, which reproduce the T dwarfs' location. Nonequilibrium effects are important in the near-infrared as gas transport leads to an enhancement of N_2 at the expense of NH_3. This increases the flux in the near-infrared, especially at H (e.g., Leggett et al. 2016b), hence the better fit to $J-H$ by the T15 models. The only model that reproduces the $J-K$ colors of the Y dwarfs is the T15 model with the change to the adiabatic index, because of the large reduction in the J flux (Figure 1).

A comparison of the S12 and M14 sequences in Figures 10 and 11 suggests that the near-infrared colors of Y dwarfs are insensitive to clouds, although clouds may be important at the $\sim$10% level for Y dwarfs (see also Section 3). Gravity appears to be an important parameter for $J-H$ and $J-K$, and metallicity appears to be important for $Y-J$, $J-H$, and $J-K$. The interpretation of $Y-J$ is not straightforward, however, as both W0350 and W1828 appear bluer in $Y-J$ than the other Y dwarfs, while Figures 8 and 9 imply that W0350 is metal-rich and W1828 is metal-poor. Figures 10 and 11 suggest that the

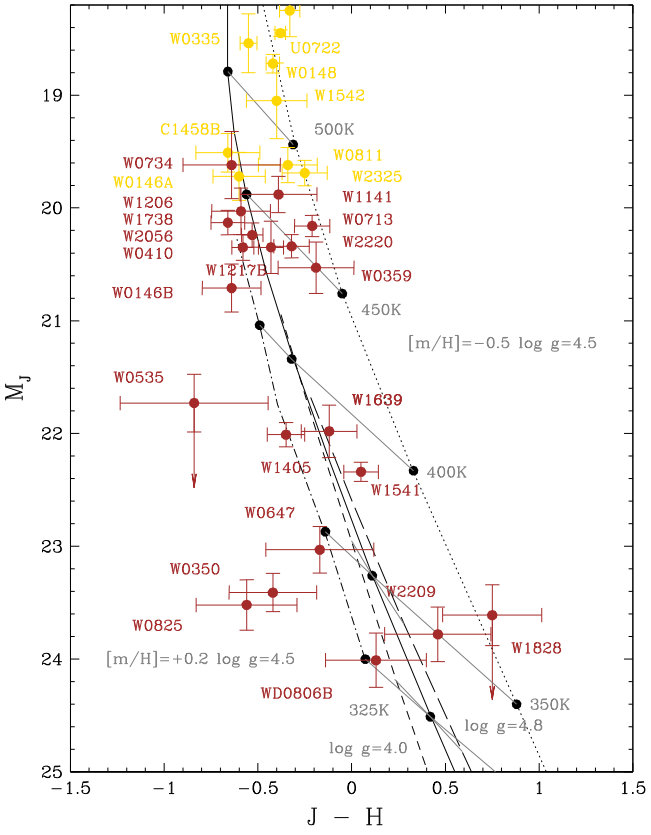

Figure 13. Absolute J as a function of $J-H$ for T9 and Y dwarfs. T15 nonequilibrium sequences are shown for solar-metallicity models with $\log g = 4.5$ (solid line), $\log g = 4.0$ (short dashed line), and $\log g = 4.8$ (long dashed line). Non-solar-metallicity sequences with $\log g = 4.5$ are also shown: $[m/H] = -0.5$ (dotted line) and $[m/H] = +0.2$ (dashed-dotted line). Values of $T_{\rm eff}$ are indicated along the sequences. W0535 and W1828 appear to be multiple sources, and the downward arrows indicate their location if they are a pair of identical Y dwarfs.

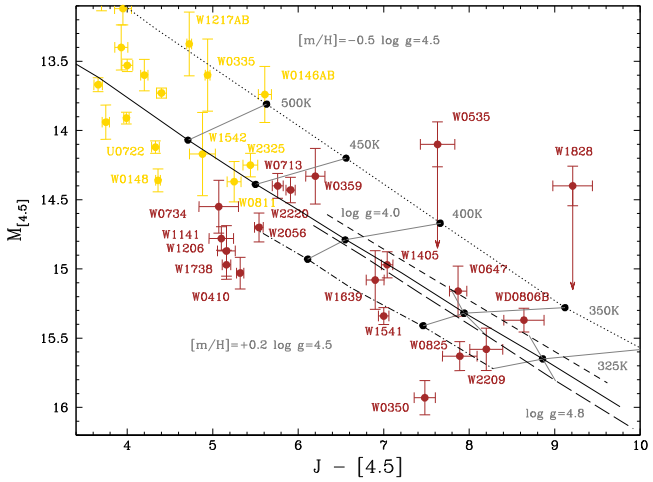

Figure 14. Absolute [4.5] as a function of $J-[4.5]$ for T9 and Y dwarfs. Lines are as in Figure 13. W0535 and W1828 appear to be multiple sources, and the downward arrows indicate their location if they are a pair of identical Y dwarfs.

W0146AB system may be metal-rich, while WISE J033515.01+431045.1 (W0335, T9) may be metal-poor.

Figure 12 shows absolute [4.5] as a function of the mid-infrared colors [3.6]−[4.5] and [4.5]−W3 (see Figure 1 for filter bandpasses). In this mid-infrared color–color space, the change of the adiabat in the T15 models does not significantly change the location of the model sequence. None of the models can reproduce the [3.6]−[4.5]:$M_{[4.5]}$ observations of the Y dwarfs, although the nonequilibrium models do a much better job of reproducing these colors for the T dwarfs. The models are mostly within 2σ of the observational error in the [4.5]−W3:$M_{[4.5]}$ plot, although there is a suggestion that for the Y dwarfs the model [4.5] fluxes are too high or the W3 fluxes are too low (see also Section 10.5).

A comparison of the S12 and M14 sequences in Figure 12 suggests that the mid-infrared colors of Y dwarfs with $M_{[4.5]} > 16$ mag, such as W0855, are sensitive to the presence of water clouds. Gravity does not appear to play a large role in these mid-infrared color–magnitude diagrams, but metallicity does. The discrepancy with observations, however, makes it difficult from this figure to constrain parameters or determine whether or not W0855 is cloudy.

In the next section we compare near-infrared spectra of Y dwarfs to synthetic spectra. The photometric comparisons have demonstrated that the late-T and Y dwarfs are mostly cloud-free and that nonequilibrium chemistry is important for interpretation of their energy distributions (see also Leggett et al. 2016b). We therefore compare the spectra to T15 models only. We use a single diffusion coefficient of $\log K_{zz} = 6$, as indicated by our M' measurements (Section 8.1). We also use only nonmodified adiabats. Although the modified adiabat produces redder colors, which in some cases agree better with observations, it does so by reducing the *YJH* flux (Figure 1). Based on the mid-infrared color–magnitude plot (Figure 12), the problem appears to be a shortfall of flux in the models at [3.6] (and K). Note that the [3.6] (and W1) filter covers a region where the flux increases sharply to the red as the very strong absorption by CH_4 decreases (Figure 1, bottom panel). A relatively small change in this slope may resolve the observed discrepancy.

9. Spectroscopy: The Sample and Comparison to Models

In this section we compare near-infrared spectra of Y dwarfs to T15 nonequilibrium cloud-free models. We analyze Y dwarfs that have trigonometric parallax measurements only so that the model fluxes can be scaled to the distance of the Y dwarf. Given the problems at K (Section 8.3), we only use the *YJH* wavelength region (most of the observed spectra only cover this region).

Figures 13 and 14 are color–magnitude plots for the known Y dwarfs and latest-T dwarfs. Sequences for the T15 solar, supersolar, and subsolar metallicity models are shown, as well as sequences for $\log g = 4.0$, 4.5, and 4.8. For this low-temperature solar-neighborhood sample, $\log g$ almost directly correlates with mass, and $T_{\rm eff}$ provides the age once $\log g$ (mass) is known (Figure 2). Figures 2 and 14 suggest that $M_{[4.5]}$ is almost directly correlated with $T_{\rm eff}$ for the Y dwarfs. This is consistent with the radii of the Y dwarfs being approximately constant and the model calculation that one-half the total flux is emitted through the [4.5] bandpass for this range of $T_{\rm eff}$ (Section 2). Figures 13 and 14 show that the T15 models indicate effectively the same value of $T_{\rm eff}$ based on M_J or $M_{[4.5]}$ for each Y dwarf. Excluding the very low luminosity W0855, the Y dwarfs have $325 \lesssim T_{\rm eff}$ (K) $\lesssim 450$.

Near-infrared spectra of 20 Y dwarfs or Y dwarf systems with trigonometric parallaxes are available from this work, Cushing et al. (2011), Kirkpatrick et al. (2012), Tinney et al.

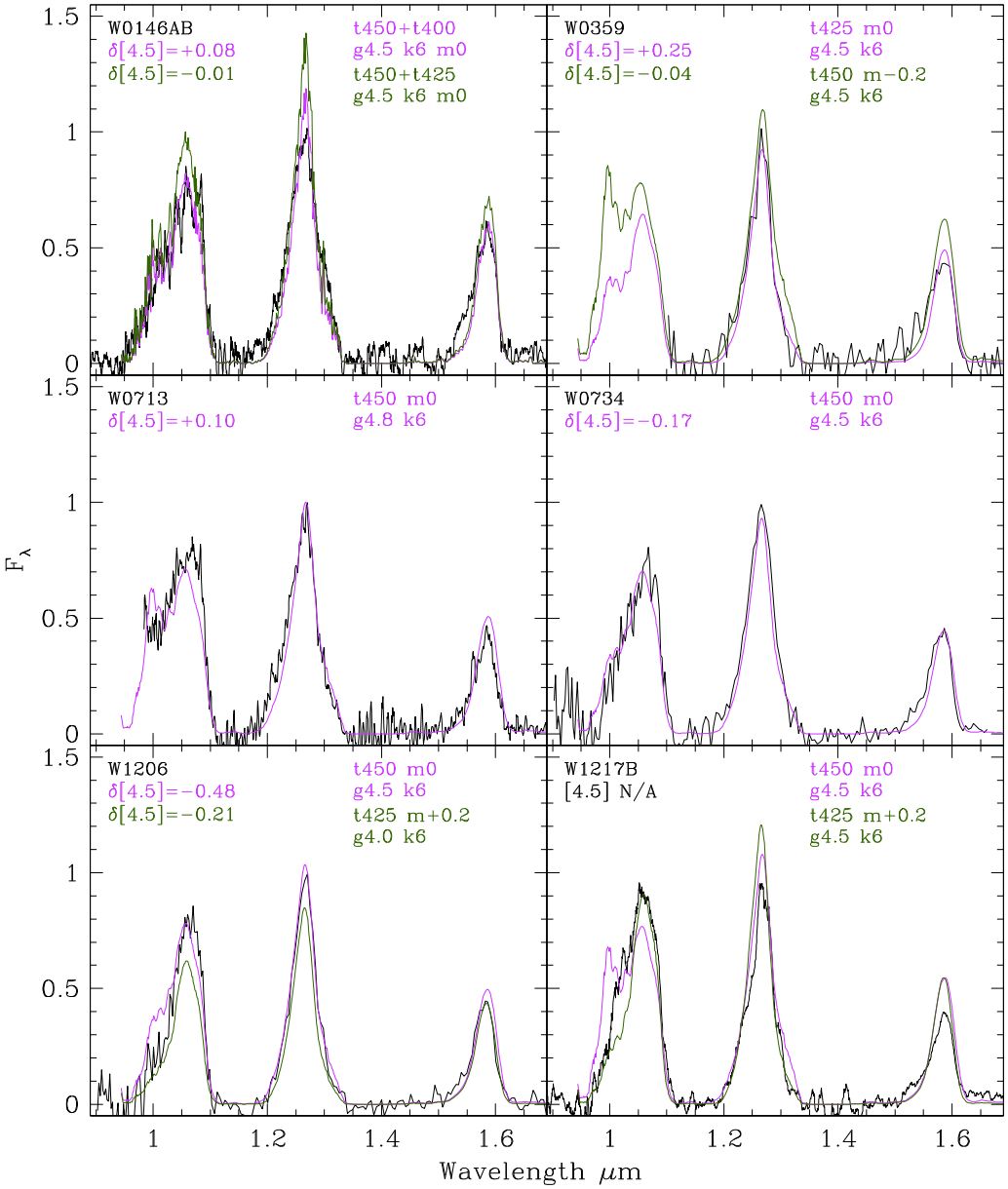

Figure 15. Tremblin et al. (2015) cloud-free nonequilibrium model fits (violet and dark green lines) to observed near-infrared spectra (black lines), with $425 \leqslant T_{\rm eff}$ (K) $\leqslant 450$. The legends give name, model parameters, and $\delta\,[4.5] = M_{[4.5]}$(model) − $M_{[4.5]}$(observed). There is no resolved [4.5] photometry for the W1217 binary system. Observed spectra are flux-calibrated by photometry; the models are flux-calibrated by the object's distance and the evolutionary radius for $T_{\rm eff}$ and $\log g$ (Saumon & Marley 2008). The spectra are normalized so the *J*-band peak is ∼1.0. The uncertainty in the flux calibration is 10%–20% (Table 8).

(2012), Kirkpatrick et al. (2013), Leggett et al. (2014, 2016b), and Schneider et al. (2015). We flux-calibrated the spectra using the observed near-infrared photometry, which has a typical uncertainty of 10%–20% (Table 8). For W0535, the flux calibration of the *H* region of the spectrum is inconsistent with the *Y* and *J* regions by a factor of four, and our fit suggests that the *H* region of the spectrum is too bright. For W1828, the flux calibrations of the *J* and *H* spectral regions differ by a factor of two. We explored fits to the spectrum using both scaling factors, and the fits suggest there is a spurious flux contribution in the shorter wavelengths of the spectrum. The color–magnitude plots imply that W0535 and W1828 are multiple systems (Section 8.2), and contemporaneous near-infrared spectroscopy and photometry would be helpful in excluding variability in these sources and enabling a more reliable spectral fit.

We compared the spectra to a set of T15 cloud-free, standard-adiabat models with $\log K_{zz} = 6$. Solar-metallicity models were computed with surface gravities given by $\log g = 4.0$, 4.5, and 4.8, for $T_{\rm eff}$ values of 300–500 K in steps of 25 K. Solar-metallicity $\log g = 3.8$ models were calculated for $T_{\rm eff} = 325$, 350, and 375 K also, which evolutionary models show are plausible for a solar neighborhood sample (Figure 2). A few metal-poor ([*m/H*] = −0.2 and −0.5) and metal-rich ([*m/H*] = +0.2, +0.3, and +0.4) models were calculated as needed when exploring individual fits. The model fluxes are converted from stellar surface flux to flux at the distance of the Y dwarf using the observed trigonometric parallax and the radius that corresponds to the $T_{\rm eff}$ and $\log g$ of the model as given by the Saumon & Marley (2008) evolutionary models. The typical uncertainty in the parallax-implied distance modulus is 10%–20% (Table 8). No other

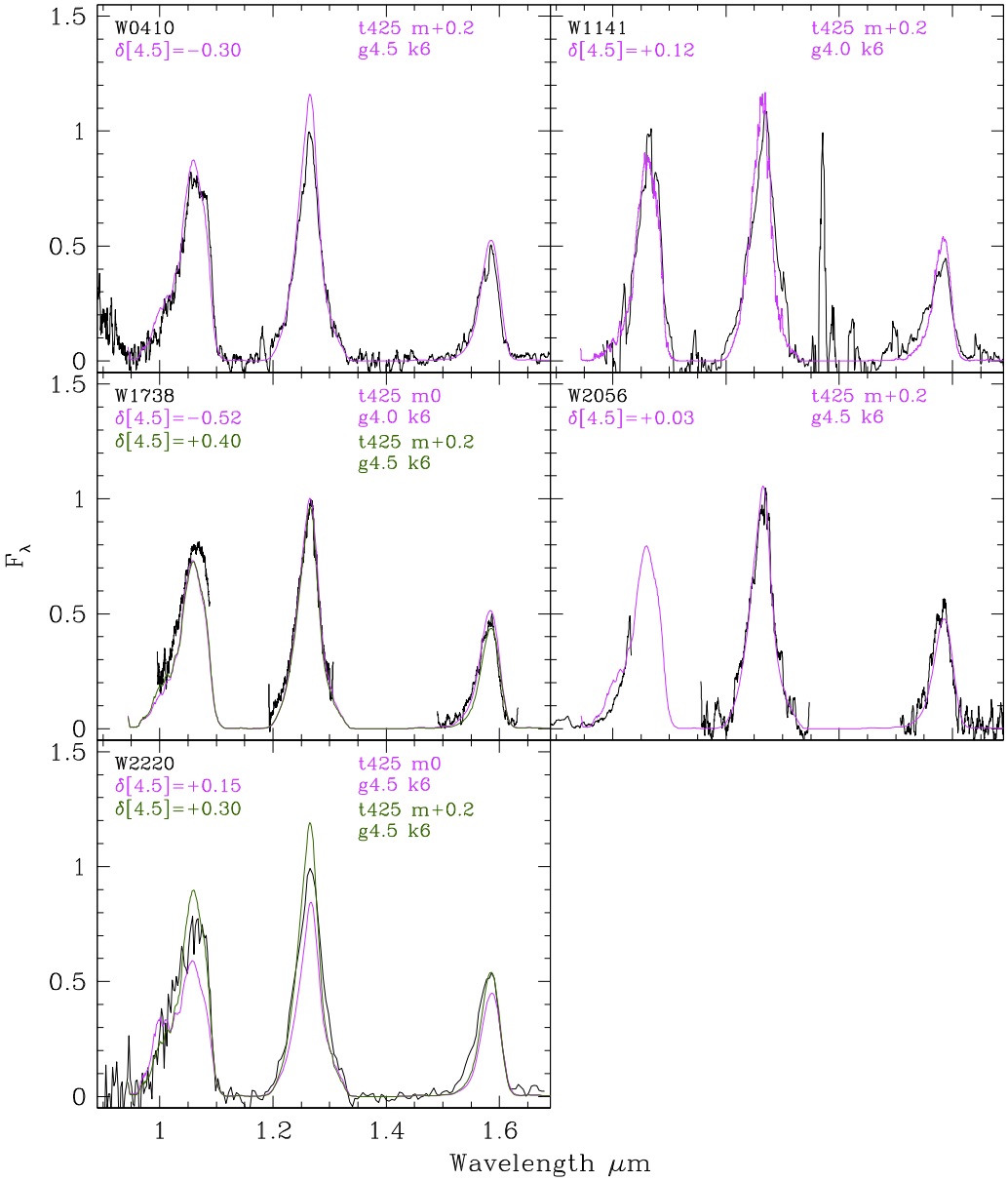

Figure 16. Tremblin et al. (2015) cloud-free nonequilibrium model fits (violet and dark green lines) to observed Y dwarf near-infrared spectra (black lines), for which we determine $T_{\rm eff}$ = 425 K. Lines are as in Figure 15.

scaling was done to the models to improve agreement with the observations.

Due to the coarse nature of our model grid and the poor S/N of most of the spectra (due to the faintness of the sources), we fit the spectra by eye only. We determined the difference between the computed and observed [4.5] magnitude as a further check of the validity of the selected models. The models that are preferred for the near-infrared spectral fitting give [4.5] values that are within 0.35 mag of the observed value, and on average they are within 0.15 mag of the observed [4.5] magnitude. The spectroscopic fits and δ[4.5] values support the photometrically identified non-solar-metallicity values for W0350 (metal-rich), W0359 (metal-poor), and W1828 (metal-poor) (Section 8.2).

Our selected fits for the sample of 20 Y dwarfs are shown in Figures 15–18, where the spectra are grouped by $T_{\rm eff}$. For several of the Y dwarfs, we show two fits that straddle the observations. Those multiple fits indicate that the uncertainty in the derived $T_{\rm eff}$, log g, and [m/H] is approximately one-half the model grid spacing: $\pm$15 K, $\pm$0.25 dex, and $\pm$0.15 dex, respectively. Better fits could be determined with a finer grid of models and a least-squares type of approach, but this would only be worthwhile when higher S/N spectra are available.

Overall, the fits to the warmer half of the sample, with $425 \leqslant T_{\rm eff}$ (K) $\leqslant 450$, are very good. For the cooler half of the sample, with $325 \leqslant T_{\rm eff}$ (K) $\leqslant 375$, the model spectra appear to be systematically too faint in the Y band or, alternatively, too bright at J and H. The discrepancy may be associated with the formation of water clouds, which are expected to become important at these temperatures and which are not included in the T15 models. We discuss this further in Section 10.5.

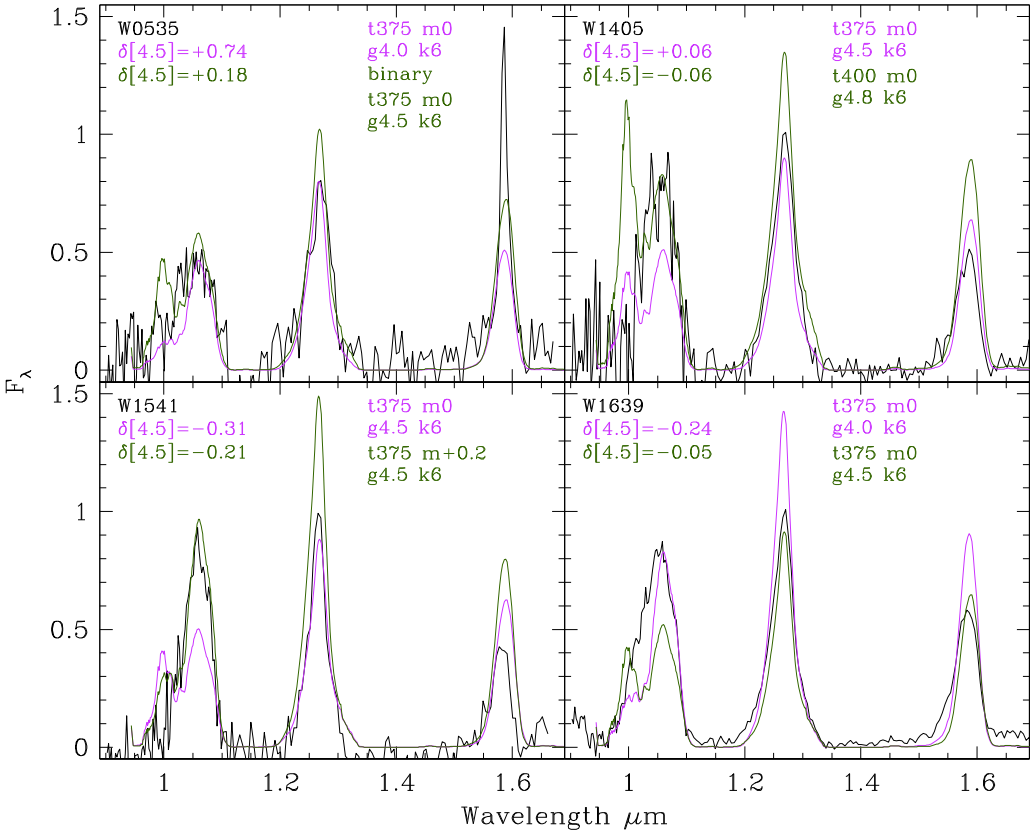

Figure 17. Tremblin et al. (2015) cloud-free nonequilibrium model fits (violet and dark green lines) to observed Y dwarf near-infrared spectra (black lines), for which we determine $375 \leqslant T_{\rm eff}$ (K) $\leqslant 400$. Lines are as in Figure 15. For W0535, the binary solution is preferred due to the better agreement with $M_{[4.5]}$. For this Y dwarf, the *H*-band flux calibration is inconsistent with *Y* and *J*, and we suggest that there are spurious, bright data points in the *H* region of the spectrum.

10. Properties of the Y Dwarfs

Table 9 gives the estimated properties of the sample of 24 Y dwarfs, based on near-infrared spectra and photometry, or photometry only if there is no spectrum available, or in one case the photometry and the properties of its companion. Mass and age are estimated from $T_{\rm eff}$ and $\log g$ using the evolutionary models of Saumon & Marley (2008, Figure 2), allowing for uncertainty in the temperature and gravity determinations. Table 9 also lists the tangential velocities ($v_{\rm tan}$) for the Y dwarfs with parallax measurements. Dupuy & Liu (2012, their Figure 31) use a Galaxy model to show that low-mass dwarfs with $v_{\rm tan} < 80\,{\rm km\,s^{-1}}$ are likely to be thin disk members, and those with $80 < v_{\rm tan}\,({\rm km\,s^{-1}}) < 100$ may be either thin or thick disk members. Twenty-one of the 22 Y dwarfs with $v_{\rm tan}$ measurements have $v_{\rm tan} < 80\,{\rm km\,s^{-1}}$; the remaining Y dwarf, the very low-temperature W0855, has $v_{\rm tan} = 86\,{\rm km\,s^{-1}}$. There is significant overlap in the Galactic populations in kinematics, age, and metallicity, but generally the thin disk is considered to be younger than ∼7 Gyr and has a metallicity $-0.3 \lesssim {\rm [Fe/H]} \lesssim +0.3$, while the thick disk is older than ∼9 Gyr and has $-1.0 \lesssim {\rm [Fe/H]} \lesssim -0.3$ (e.g., Bensby et al. 2014).

Leggett et al. (2016b) compare near-infrared spectra and photometry to T15 models for three Y dwarfs in common with this work: W0350, W1217B, and W1738. The technique used is similar to that used here (although fewer models were available), and the derived $T_{\rm eff}$ and $\log g$ are in agreement, given our new determination for the distance to W0350. Schneider et al. (2015) compare *HST* near-infrared spectra and *Spitzer* mid-infrared photometry for a set of Y dwarfs to the S12, M12, and M14 solar-metallicity equilibrium chemistry models. A goodness-of-fit parameter is used that incorporates the distance and evolutionary radius associated with the model parameters. As stated by Schneider et al., the fits to the data are poor in many cases. This is likely due to a combination of the omission of chemical nonequilibrium in the models and poorly constrained parallaxes for some of the Y dwarfs. The range in the Schneider et al. temperature and gravity values for each Y dwarf is about twice that derived here. There is generally good agreement between our values and those of Schneider et al. Of the sample of 16 objects in common, only five have $T_{\rm eff}$ or $\log g$ values that differ by more than the estimated uncertainty. For two of these, we use different values for the parallax (W0535 and W0825); for another pair (W0647 and WISEA J163940.84−684739.4 (W1639)), the $T_{\rm eff}$ values are consistent but the Schneider et al. gravities are significantly higher; and for the remaining object (WISEA J220905.75+271143.6 (W2209)), Schneider et al. obtain a much higher temperature. For the last three Y dwarfs, the higher gravities or temperature are unlikely, based on age and luminosity arguments.

We discuss our results in terms of populations and also discuss individual Y dwarfs of particular interest in the following subsections. Two Y dwarfs without trigonometric parallax measurements are not discussed further: W0304 and WISEA J235402.79+024014.1. Two T9 dwarfs appear to have significantly nonsolar metallicity and should be followed up: WISE J041358.14−475039.3 (metal-rich) and WISEPA J075108.79−763449.6 (metal-poor).

10.1. Likely Young, Metal-rich Y Dwarfs

Five Y dwarfs have low tangential velocities of $8 \leqslant v_{\rm tan}\,({\rm km\,s^{-1}}) \leqslant 40$, appear to be metal-rich, and also have an age $\lesssim$3 Gyr as estimated from $T_{\rm eff}$ and $\log g$. These are

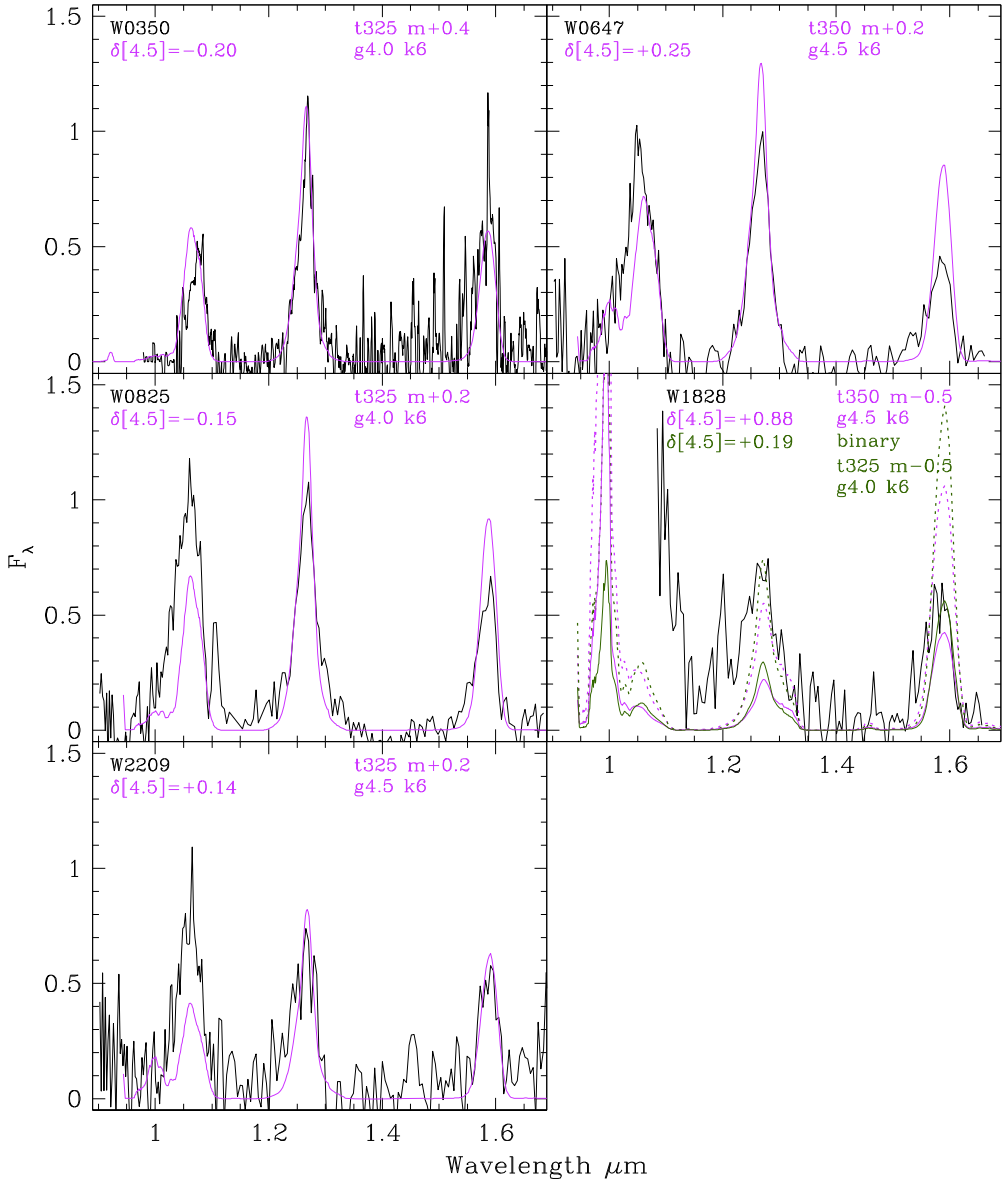

Figure 18. Tremblin et al. (2015) cloud-free nonequilibrium model fits (violet and dark green lines) to observed Y dwarf near-infrared spectra (black lines), with $325 \leqslant T_{\rm eff}$ (K) $\leqslant 350$. Lines are as in Figure 15. For W1828, the *J*- and *H*-band flux calibrations are inconsistent. The solid violet and dark green lines show the fits assuming that the *H*-band region of the spectrum and the *H* photometry are correct, and the dotted line shows the same models if the *J*-band spectrum and photometry are correct. It appears that the observed spectrum may include a spurious signal at $\lambda < 1.35$ μm.

W0350, W0825, W1141, W1206, and W1738. They also appear to be low-mass ∼8 Jupiter-mass objects.

10.2. Likely Solar-age and Solar-metallicity Y Dwarfs

Fourteen Y dwarfs have kinematics, metallicities, and age, as implied by $T_{\rm eff}$ and $\log g$, that suggest they are generally solar-like in age and chemistry. These have estimated ages of 3–8 Gyr and masses of 10–20 Jupiter masses: W0146B, W0359, W0410, W0535 (if an equal-mass binary), W0647, W0713, WISE J073444.02−715744.0 (W0734), W1217B, W1405, W1541, W1639, W2056, W2209, and W2220. All these Y dwarfs have a tangential velocity and estimated age consistent with thin disk membership, although W0713 and W2209 have upper limits on their age of 12 and 15 Gyr, respectively.

10.3. WISEPA J182831.08+265037.8

The superluminosity of W1828 in the color–magnitude diagrams does not seem explainable by any other means than binarity. The selected model in the case of W1828 being an equal-mass binary implies that this system is relatively young. It would be composed of two ∼6 Jupiter-mass objects and have an age of ∼1.5 Gyr. The *HST* images imply that the binary separation is $\lesssim$2 au (Section 8.2). An age of 1.5 Gyr is notionally at odds with the apparently very metal-poor nature of the system.

A better near-infrared spectrum and a mid-infrared spectrum when the *James Webb* telescope is online should improve our understanding of this Y dwarf. Exploration of a nonidentical binary pair solution would also be worthwhile once a better spectrum is available.

10.4. WD0806−661B

The primary of this binary system, WD0806−661A, is a helium-rich DQ-class white dwarf separated from the brown dwarf by 2500 au (Luhman et al. 2011). Hydrogen-deficient post-asymptotic-giant-branch (AGB) stars may evolve into DB

Table 8
Y Dwarf Data Set

Name(R.A.) (Decl.)	Spectral Type	$M - m$(err) [3.6](err)	Y(err) [4.5](err)	J(err) W1(err) magnitudes	H(err) W2(err)	K(err) W3(err)	Ref(π) Ref([3.6][4.5])	Ref($YJHK$) Ref(Discovery)
WISE J014656.66[a]	Y0	−1.34(20)	22.85(19)	22.05(7)	22.69(14)	⋯	Table 7	D15
+423410.0B		⋯	⋯	⋯	⋯	⋯		K12, D15
WISE J030449.03	Y0	⋯	21.32(17)	20.79(09)	21.02(16)	⋯		P14, Table 4
−270508.3		17.71(03)	15.48(03)	⋯	15.59(09)	⋯	Table 3	P14
WISEA J035000.31	Y1	1.32(12)	21.62(12)	22.09(10)	22.51(20)	⋯	LE16	L15
−565830.5		17.84(03)	14.61(03)	⋯	14.75(04)	12.33(28)	L15	K12
WISE J035934.06	Y0	−1.00(20)	21.84(11)	21.53(11)	21.72(17)	22.80(30)	T14	L15
−540154.6		17.55(07)	15.33(02)	19.10(20)	15.38(05)	14.00(20)	K12	K12
WISEA J041022.75	Y0	0.91(11)	19.61(04)	19.44(03)	20.02(05)	19.91(07)	B14	L13
+150247.9		16.56(03)	14.12(03)	⋯	14.11(05)	12.31(50)	L13	C11
WISE J053516.80	⩾Y1	−0.77(16)	22.73(30)	22.50(20)	23.34(34)	⋯	Table 7	L15
−750024.9		17.54(03)	14.87(03)	17.94(14)	14.90(05)	⋯	L15	K12
WISE J064723.23	Y1	0.09(18)	23.13(09)	22.94(10)	23.11(27)	⋯	T14	L15, Table 1
−623235.5		17.89(09)	15.07(02)	⋯	15.22(05)	⋯	K13	K13
WISE J071322.55	Y0	0.18(08)	20.34(08)	19.98(05)	20.19(08)	21.30(30)	B14	L15
−291751.9		16.67(05)	14.22(04)	⋯	14.46(05)	12.29(36)	B14	K12
WISE J073444.02	Y0	−0.66(19)	21.02(05)	20.05(05)	20.92(12)	20.96(15)	B14	L15
−715744.0		17.69(08)	15.21(02)	18.75(28)	15.19(05)	⋯	K12	K12
WD 0806	Y1	−1.41(07)	25.14(22)	25.42(23)	25.29(14)	⋯	S09	Table 6
−661B		19.28(10)	16.78(05)	⋯	16.88(05)	⋯	L15	LBB11
WISEA J082507.37	Y0.5	0.99(10)	22.66(11)	22.53(10)	23.09(18)	⋯	LE16	Table 6
+280548.2		17.62(08)	14.64(03)	⋯	14.58(06)	⋯	S15	S15
WISE J085510.83[b]	>Y2	3.26(04)	26.54(21)	25.45(24)	23.83(24)	⋯	LE16	Table 6
−071442.5		17.31(03)	13.87(04)	17.82(33)	14.02(05)	11.90(30)	LE16	L14
WISEA J114156.67	Y0	0.12(08)	20.33(14)	19.76(14)	20.15(15)	⋯	T14	T14, Table 6
−332635.5		16.64(08)	14.66(03)	17.08(12)	14.61(06)	11.73(21)	Table 3	T14
WISEA J120604.25	Y0	−0.35(18)	20.89(10)	20.38(10)	20.97(12)	⋯	LE16	Table 6
+840110.5		17.34(06)	15.22(03)	⋯	15.06(06)	⋯	S15	S15
WISEPC J121756.91[a]	Y0	0.27(23)	20.26(03)	20.08(03)	20.51(06)	21.10(12)	Table 7	L12
+162640.2B		⋯	⋯	⋯	⋯	⋯		K12, L12
WISEPC J140518.40	Y0.5	0.95(09)	21.24(10)	21.06(06)	21.41(08)	21.61(12)	Table 7	L13
+553421.5		16.78(03)	14.02(03)	18.77(40)	14.10(04)	12.20(26)	L13	C11
WISE J154151.65	Y1	1.22(06)	21.46(13)	21.12(06)	21.07(07)	21.70(20)	B14	L13, L15
−225024.9		16.92(02)	14.12(02)	⋯	14.25(06)	12.20(30)	L13	C11
WISEA J163940.84	Y0pec	1.51(21)	20.54(10)	20.47(10)	20.59(11)	⋯	T14	Table 6
−684739.4		16.23(03)	13.57(03)	17.27(19)	13.54(06)	⋯	Table 3	T12
WISEA J173835.52	Y0	0.55(10)	19.74(08)	19.58(04)	20.24(08)	20.58(10)	B14	L16b
+273258.8		16.87(03)	14.42(03)	17.71(16)	14.50(04)	12.45(40)	L16b	C11
WISEPA J182831.08	⩾Y2	0.13(14)	23.03(17)	23.48(23)	22.73(13)	23.48(36)	B14	L13, L15
+265037.8		16.84(03)	14.27(03)	17.34(26)	14.35(05)	12.44(34)	L13	C11
WISEA J205628.88[b]	Y0	0.81(10)	19.77(05)	19.43(04)	19.96(04)	20.01(06)	B14	L13
+145953.6		16.06(10)	13.89(03)	16.48(08)	13.84(04)	11.73(25)	Table 3, L13	C11
WISEA J220905.75	Y0	0.84(15)	23.04(12)	22.94(19)	22.48(21)	⋯	B14	Table 6
+271143.6		17.82(09)	14.74(03)	⋯	14.77(06)	12.46(39)	C14	C14
WISE J222055.31	Y0	−0.30(09)	20.91(09)	20.64(05)	20.96(08)	21.33(15)	B14	L15
−362817.4		17.20(06)	14.73(02)	⋯	14.71(06)	⋯	K12	K12
WISEA J235402.79	Y1	⋯	⋯	22.72(13)	22.53(38)	⋯		Table 6
+024014.1		18.11(11)	15.01(02)	⋯	15.01(09)	⋯	S15	S15

Notes. Photometric error is in centimag. W1, W2, and W3 photometry is from the ALLWISE catalog.
[a] WISE J014656.66+423410.0B and WISEPC J121756.91+162640.2B are in close binary systems. Mid-infrared photometry is not available for the individual components of the systems.
[b] We have also measured for WISE J085510.83−071442.5 $M' = 13.95 \pm 0.20$ mag and for WISEA J205628.88+145953.6 $M' = 14.00 \pm 0.15$ mag.
References. Beichman et al. (2014), Cushing et al. (2011, 2014), Dupuy et al. (2015), Kirkpatrick et al. (2012, 2013), Leggett et al. (2013; 2015; 2016b), Liu et al. (2012), Luhman et al. (2011), Luhman (2014), Luhman & Esplin (2016), Pinfield et al. (2014), Schneider et al. (2015), Subasavage et al. (2009), Tinney et al. (2012, 2014).

(helium-rich white dwarfs) and then DQ white dwarfs (Althaus et al. 2005; Dufour et al. 2005). Calculations of the late stages of AGB evolution can produce the less common non-DA (non-hydrogen-rich) white dwarfs in about the correct proportion, although there are multiple paths that lead to hydrogen deficiency (Lawlor & MacDonald 2006). One factor in these AGB evolution models is the metallicity of the star, and it is possible that the subsolar metallicity we find for the Y dwarf WD0806−661B is related to the DQ (i.e., non-DA) nature of the primary. Table 9 gives the properties of this Y dwarf, using

Table 9
Y Dwarf Estimated Properties

Name	Type	v_{tan} (km s^{-1})	[*m/H*]	T_{eff} (K)	log *g* (cm s^{-2})	Mass (Jupiter)	Age (Gyr)
WISE J014656.66+423410.0B	Y0	40(4)	∼0	400–430	4.25–4.75	8–20	0.8–7
WISE J030449.03−270508.3[a]	Y0	…	≲0	450–500	…	…	…
WISEA J035000.31−565830.5	Y1	16(1)	+0.25–+0.55	310–340	3.75–4.25	3–8	0.3–3
WISE J035934.06−540154.6	Y0	57(18)	−0.25–+0.05	420–450	4.25–4.75	8–20	0.7–6
WISEA J041022.75+150247.9	Y0	72(4)	0–+0.3	410–440	4.25–4.75	8–20	0.8–6
WISE J053516.80−750024.9[b]	⩾Y1	9(1)	−0.15–+0.15	360–390	4.25–4.75	8–20	1–10
WISE J064723.23−623235.5	Y1	19(7)	−0.05–+0.25	320–350	4.0–4.5	5–13	0.8–6
WISE J071322.55−291751.9	Y0	26(3)	−0.15–+0.15	435–465	4.5–5.0	13–29	2–12
WISE J073444.02−715744.0	Y0	37(11)	−0.15–+0.15	435–465	4.25–4.75	9–20	0.8–5
WD 0806−661B[c]	Y1	41(1)	<0	325–350	4.2–4.3	7–9	1.5–2.7
WISEA J082507.37+280548.2	Y0.5	8(1)	0–+0.3	310–340	3.75–4.25	3–8	0.3–3
WISE J085510.83−071442.5[d]	>Y2	86(3)	−0.2–+0.2	240–260	3.5–4.3	1.5–8	0.3–6
WISEA J114156.67−332635.5	Y0	41(8)	0–+0.3	410–440	3.75–4.25	3–8	0.1–1.0
WISEA J120604.25+840110.5	Y0	36(3)	−0.05–+0.25	420–450	4.0–4.5	6–14	0.4–3
WISEPC J121756.91+162640.2B	Y0	62(6)	−0.05–+0.25	420–450	4.25–4.75	8–20	0.7–6
WISEPC J140518.40+553421.5[d]	Y0.5	72(3)	−0.15–+0.15	370–400	4.3–4.8	9–21	1.5–10
WISE J154151.65−225024.9	Y1	23(1)	−0.05–+0.25	360–390	4.25–4.75	8–20	1–10
WISEA J163940.84−684739.4	Y0pec	74(9)	−0.15–+0.15	360–390	4.0–4.5	5–14	0.5–5
WISEA J173835.52+273258.8[d]	Y0	17(1)	−0.05–+0.25	410–440	4.0–4.5	5–14	0.3–3
WISEPA J182831.08+265037.8[b]	⩾Y2	46(3)	−0.6–−0.3	310–340	3.75–4.25	3–8	0.3–3
WISEA J205628.88+145953.6	Y0	33(2)	0–+0.3	410–440	4.25–4.75	8–20	0.8–6
WISEA J220905.75+271143.6	Y0	59(4)	0–+0.3	310–340	4.25–4.75	8–19	2–15
WISE J222055.31−362817.4	Y0	10(1)	−0.05–+0.25	410–440	4.25–4.75	8–20	0.8–6
WISEA J235402.79+024014.1[e]	Y1	…	∼0	∼350	…	…	…

Notes. For Y dwarfs with near-infrared spectroscopy, the estimated uncertainty in T_{eff}, log *g*, and [*m/H*] is ±15 K, ±0.25 dex, and ±0.15 dex (Figures 15–18, see text).

[a] The color–color plots *J*−[4.5]:[3.6]−[4.5] and *J*−[4.5]:*J* − *H* suggest W0304 is slightly metal-poor. The temperature is estimated from the *J*−[4.5] color, assuming the metallicity is solar or subsolar.

[b] W0535 and W1828 appear to be similar-mass binary systems based on the color–magnitude plots. The estimated properties assume these are same-mass binary systems.

[c] The white dwarf primary constrains the age of the system (Rodriguez et al. 2011). The brown dwarf appears significantly metal-poor in the *J*−[4.5]:[3.6]−[4.5] plot. The temperature is estimated from M_J:*J* − *H* and $M_{[4.5]}$:*J*−[4.5], and T_{eff} and age together constrain gravity and mass.

[d] Rotation periods based on variability are for W0855 5–16 hr (Luhman & Esplin 2016), for W1405 8.5 hr (Cushing et al. 2016), and for W1738 6.0 hr (Leggett et al. 2016a). Brown dwarfs are expected to spin up with time such that brown dwarfs younger than around 10 Myr would have a period of 14–48 hr (Bouvier et al. 2014).

[e] The color–color plots *J*−[4.5]:[3.6]−[4.5] and *J*−[4.5]:*J* − *H* suggest W2354 has solar metallicity. The temperature is estimated from *J*−[4.5] color, assuming solar metallicity.

the white dwarf primary to constrain the age of the system to 1.5–2.7 Gyr (Rodriguez et al. 2011).

10.5. WISE J085510.83−071442.5

Figure 19 shows the photometric data points observed for W0855 as fluxes as a function of wavelength. Table 8 lists *YJH*, [3.6], [4.5], W1, W2, and W3 magnitudes for W0855. *YJH* were derived by us from *HST* photometry (Section 6, Table 6). The [3.6] and [4.5] are from LE16, the W1 and W2 magnitudes are from the *WISE* catalog, and W3 was determined here from *WISE* images (Section 5.4, Table 3). Also shown are shorter wavelength data points from LE16: LP850 obtained using the *HST* Advanced Camera for Surveys (ACS) and the *i*-band upper limit obtained using GMOS at Gemini South.

Model spectra are shown for comparison, all with T_{eff} = 250 K. Models with T_{eff} = 225 K produce too little flux at 5 μm, and models with T_{eff} = 275 K produce too much flux at 5 μm, by a factor of 1.5. The models show that ∼40% of the total flux is emitted through the [4.5] bandpass and ∼30% through the W3 bandpass. An additional ∼20% is emitted at $19 < \lambda(\mu m) < 28$ (the W4 bandpass), and ∼5% at $\lambda > 30\,\mu m$. Less than 1% of the total flux is emitted at $\lambda < 4\,\mu m$. The effective temperature (or luminosity) is tightly constrained by the mid-infrared flux, and we estimate that for W0855 $T_{eff} = 250 \pm 10$ K. This is consistent with previous studies (Beamin et al. 2014; Luhman 2014; Leggett et al. 2015; Schneider et al. 2016; Zapatero Osorio et al. 2016).

We compared several models to the SED. T15 models were calculated with log *g* = 3.5, 3.8, 4.0, 4.3, and 4.5. T15 models with T_{eff} = 250 K and nonsolar metallicities of [*m/H*] = −0.2 and +0.2 were also calculated. Finally, T15 models were calculated with log K_{zz} = 6, 8, and 9, as Figure 7 suggests that W0855 may be undergoing more chemical mixing than the warmer Y dwarfs, and Jupiter's atmosphere has been modeled with a vertical diffusion coefficient of log K_{zz} = 8 (Wang et al. 2015). The top panel of Figure 19 demonstrates the effect of varying K_{zz}, and the central panel shows models with different gravities.

We also compared the observations to M14 cloud-free and partly cloudy models that are in chemical equilibrium. These are shown in the bottom panel of Figure 19. Cloud-free models with solar metallicity and log *g* = 3.5 and 4.0 were calculated, as well as a log *g* = 4.0 solar-metallicity model with thin cloud decks (parameterized by f_{sed} = 7) covering 50% of the surface. The models are updated versions of the models published in

Table 10
WISE J085510.83−071442.5 $T_{\rm eff}$ = 250 K Model Photometric Comparison

Family[a]	log g	[m/H]	Cloud Cover[b]	log K_{zz}[c]	δY	δJ	δH	δ[4.5]	δW3
M14	4.0	0.0	nc	0	−0.35	−0.16	+1.11	−0.25	+0.45
M14	4.0	0.0	$f_{\rm sed}$ = 7 h = 50%	0	−1.94	−1.58	+0.29	−0.05	+0.07
T15	4.3	0.0	nc	9	−0.09	+0.36	+0.62	−0.18	+0.49
T15	3.8	+0.2	nc	9	−0.32	−0.61	+0.49	−0.15	−0.05
T15	3.5	0.0	nc	9	+0.14	−0.12	+0.72	−0.25	−0.04

Notes. δ = M (model) − M (observed).
[a] Models are from Tremblin et al. (2015) or updated Morley et al. (2014).
[b] Models are cloud-free (nc) or have thin cloud decks with half the surface covered ($f_{\rm sed}$ = 7 h = 50%).
[c] The parameter K_{zz} is the diffusion coefficient, and log K_{zz} = 0 implies that the models exclude mixing and are in chemical equilibrium.

Morley et al. (2014). The new models include updates to both chemistry and opacities, which will be described in detail in an upcoming paper (M. S. Marley et al. 2017, in preparation). Briefly, the opacities are as described in Freedman et al. (2014) with the exception of the CH_4 and alkali opacities; CH_4 line lists have been updated using Yurchenko & Tennyson (2014), and the alkali line lists have been updated to use the results from Allard et al. (2005). The chemical equilibrium calculations are based on previous thermochemical models (Lodders & Fegley 2002; Visscher et al. 2006; Visscher 2012) and have been revised and extended to include a range of metallicities.

Up to this point in our analysis, we have neglected the $\lambda < 0.9\,\mu$m region. Given the importance of W0855 and the availability of shorter wavelength data, Figure 19 includes observations and model spectra and photometry at $0.8 \lesssim \lambda\,(\mu{\rm m}) \lesssim 0.9$. The models are about an order of magnitude too bright at $\lambda < 0.9\,\mu$m, with the T15 models more discrepant than the modified M14 models. At the temperatures and pressures that are likely in the W0855 photosphere, H_2S is a significant opacity source at $\lambda \lesssim 0.9\,\mu$m (M14, their Figures 7 and 8). The strength of this opacity may be dependent on the treatment of the condensation of sulfides at warmer temperatures. This issue will be explored in future work.

All of the models show the discrepancy with observations at the [3.6] bandpass noted previously in Section 8.2. At this temperature, all of the models also appear too faint at H by about a factor of two. Increasing the mixing coefficient from log K_{zz} = 6 to 9 improves the agreement at YJH by 10%–15%, and at [4.5] and W3 by 5%. The addition of water clouds improves the agreement at H but makes Y and J too bright by about an order of magnitude. While the addition of water clouds and associated brightening at Y and J may improve the model fits for the $T_{\rm eff} \approx 350$ K Y dwarfs (Figures 17 and 18), at 250 K the addition of water clouds (as currently modeled) does not improve the fit in the near-infrared. We note that condensation of NH_3 is not expected until lower temperatures of ∼200 K are reached. Esplin et al. (2016) have detected variability at [3.6] and [4.5] for W0855, at the ∼4% (peak-to-peak) level. Similar variability is seen in two Y dwarfs that are too warm for water clouds, although they may have low-lying sulfide clouds (Cushing et al. 2016; Leggett et al. 2016a). Skemer et al. (2016) present a 5 μm spectrum for W0855 that suggests that water clouds are present. No analysis yet has robustly confirmed the presence of clouds in the W0855 atmosphere (Esplin et al. 2016), and new models are needed that better reproduce the SED of W0855 before their presence or absence can be confirmed.

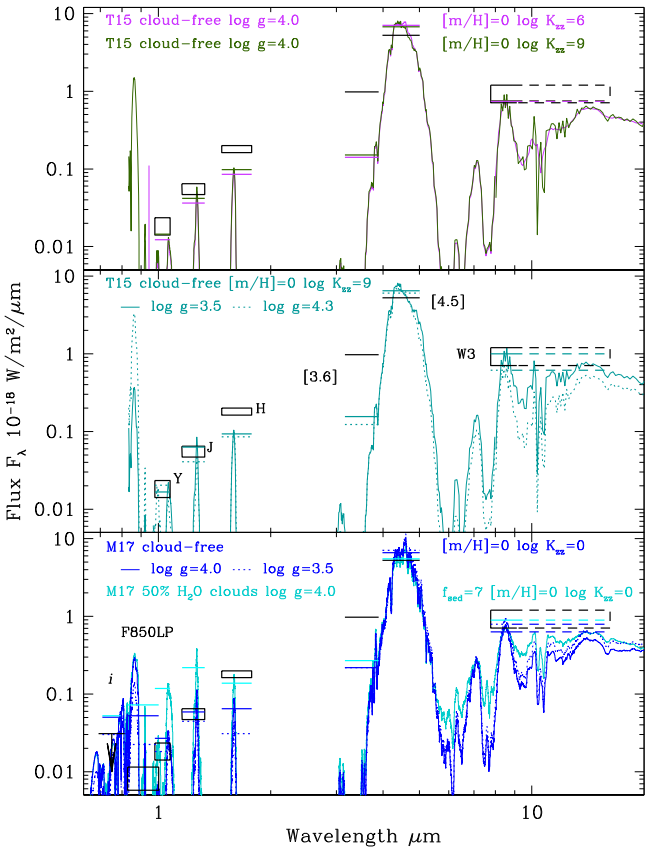

Figure 19. Observed photometry for W0855, if at 10 pc, is shown as black boxes. The box height indicates the flux uncertainty, and the box width the filter bandpass. The dashed extension for the W3 filter indicates that the flux is expected primarily at the blue end. The uncertainties in the [3.6] and [4.5] fluxes are small, and these appear as black lines. In the bottom panel, the $i_{\rm AB}$ flux is an upper limit only. Colored lines are $T_{\rm eff}$ = 250 K model spectra and photometry, as described in the legends. The model fluxes have been scaled to 10 pc and the evolutionary value of the Y dwarf radius. The top panel compares T15 models that differ in K_{zz}, the middle panel compares T15 models that differ in g, and the bottom panel compares updated M14 cloudy and cloud-free equilibrium models. See text and Table 10.

About 70% of the total flux from W0855 emerges through the [4.5] and W3 filters, and it is important therefore that the models reproduce the observed [4.5] and W3 magnitudes. However, Figure 12 suggests that there is a systematic offset between the modeled and observed values of [4.5] − W3. The analysis presented here has shown good agreement between observations and models at [4.5] (Figures 7, 9, 14), which suggests that the calculated values of W3 may be ∼0.5 mag too faint. The uncertainty in the measured [4.5] and W3

magnitudes for W0855 are 0.04 and 0.30 mag, respectively. We restrict models of the W0855 energy distribution to those where the difference $\delta = M$ (model) $- M$ (observed) magnitude is such that $-0.25 \leqslant \delta$([4.5]) $\leqslant +0.25$ and $-0.3 \leqslant \delta$ (W3) $\leqslant +0.6$. Table 10 lists the M14 and T15 models considered here that satisfy those criteria.

We find that current models imply that the 250 K Y dwarf W0855 is undergoing vigorous mixing, has a metallicity within ~0.2 dex of solar, has little or no cloud cover, and has a range in surface gravity of $3.5 \lesssim \log g \lesssim 4.3$. The Saumon & Marley (2008) evolutionary models then give a mass range of 1.5–8 Jupiter masses and an age range of 0.3–6 Gyr (Table 9). The relatively high tangential velocity of W0855 of 86 ± 3 km s^{-1} suggests the higher age (and higher mass) may be more likely.

11. Conclusion

We present new Gemini near-infrared spectroscopy for three Y dwarfs, near-infrared photometry for two Y dwarfs, and 5 μm photometry for four late-T and two Y dwarfs. We also present new near- and mid-infrared photometry for 19 T6.5 and later-type brown dwarfs, including eight Y dwarfs, using archived images. We have determined improved astrometry for four Y dwarfs, also by using archived images. Combining the new photometry with data taken from the literature allows us to transform CH_4(short) and WFC3 photometry onto MKO *YJH*. We give a newly homogenized photometric data set for the known Y dwarfs (Table 8) that enables better comparisons to models as well as the identification of trends and outliers.

Using MKO system color–magnitude diagrams and the new parallaxes, we find that two of the Y dwarfs are likely to be binaries composed of similar-mass objects: W0535 and W1828 (Figures 9, 14). WFC3 and Gemini adaptive optics images of W0535 from Opitz et al. (2016) do not resolve W0535. WFC3 images of W1828 show a marginal elongation and ellipticity of $16 \pm 8\%$. The separations of the putative binaries are $\lesssim$2 au for W1828 and <1 au for W0535.

The models show that the $J - [4.5]$:$[3.6] - [4.5]$ and the $J - [4.5]$:$M_{[4.5]}$ diagrams can be used to estimate metallicity (Figures 8, 9). We refine our atmospheric parameter estimates by comparing near-infrared spectra for 20 of the Y dwarfs to synthetic spectra generated by cloud-free nonequilibrium chemistry models (Figures 15–18). We find that all of the known Y dwarfs have metallicities within 0.3 dex of solar, except for W0350, which has [*m/H*] ~ +0.4 dex, and W1828, which has [*m/H*] ~ −0.5 dex. All of the known Y dwarfs with measured parallaxes are within 20 pc of the Sun, and therefore solar-like metallicities are expected.

Assuming W1828 is an equal-mass binary, we derive a low gravity for the pair, which translates into a relatively young age of ≈1.5 Gyr. Notionally, this is inconsistent with the degree of metal paucity that we find, as the thin disk generally has $-0.3 \lesssim$ [Fe/H] $\lesssim +0.3$ (e.g., Bensby et al. 2014). An improved near-infrared spectrum is needed for this source, preferably taken close in time to new photometry, as the current spectrum and photometry are discrepant and variability needs to be excluded.

The atmospheric parameters determined by fitting the near-infrared spectra are consistent with the values estimated photometrically. The synthetic spectra generated by T15 nonequilibrium chemistry cloud-free models reproduce observations well for the warmer half of the sample with $425 \leqslant T_{\rm eff}$ (K) $\leqslant 450$. For the cooler Y dwarfs with $325 \leqslant T_{\rm eff}$ (K) $\leqslant 375$, the models seem consistently faint at *Y*. A comparison of models to a pseudospectrum of the 250 K W0855 shows that models with patchy clouds are brighter at *Y* than cloud-free models, and the discrepancy seen in the 1 μm flux of Y dwarfs with $T_{\rm eff} \approx 350$ K may be due to the onset of water clouds. However, the cloudy models produce too much flux at $0.8 < \lambda(\mu{\rm m}) < 1.3$ for the cooler W0855. It is unclear if there is missing opacity at lower temperatures, or if the atmosphere of this cold object is cloud-free. All of the Y dwarf atmospheres appear to be turbulent, with vertical mixing leading to nonequilibrium chemistry.

We determine masses and ages for 22 Y dwarfs from evolutionary models, based on our temperature and gravity estimates (Table 9). Approximately 90% of the sample has an estimated age of 2–6 Gyr, that is, thin-disk-like as would be expected for a local sample. W1141 appears younger, with age ~0.6 Gyr, and W0713 and W2209 appear older, with ages 7 and 8.5 Gyr, respectively. About 70% of the sample has a mass of 10–15 Jupiter masses. W0350, WD0806−661B, W0825, W0855, W1141, and W1828 (if an equal-pair binary) have masses of 3–8 Jupiter masses. W0713 appears to be a 20 Jupiter-mass Y dwarf. A larger sample is needed to constrain the shape of the mass function and the low-mass limit for star-like brown dwarf formation. We may not find more Y dwarfs, however, unless or until a more sensitive version of *WISE* is flown.

Some of the data presented in this paper were obtained from the Mikulski Archive for Space Telescopes (MAST). STScI is operated by the Association of Universities for Research in Astronomy, Inc., under NASA contract NAS5-26555. Support for MAST for non-*HST* data is provided by the NASA Office of Space Science via grant NNX09AF08G and by other grants and contracts.

This work is based on data obtained from the ESO Science Archive Facility.

This research has made use of the NASA/IPAC Infrared Science Archive, which is operated by the Jet Propulsion Laboratory, California Institute of Technology, under contract with the National Aeronautics and Space Administration.

This publication makes use of data products from the Wide-field Infrared Survey Explorer, which is a joint project of the University of California, Los Angeles, and the Jet Propulsion Laboratory/California Institute of Technology, funded by the National Aeronautics and Space Administration. This research has made use of the NASA/IPAC Infrared Science Archive, which is operated by the Jet Propulsion Laboratory, California Institute of Technology, under contract with the National Aeronautics and Space Administration.

The Center for Exoplanets and Habitable Worlds is supported by the Pennsylvania State University, the Eberly College of Science, and the Pennsylvania Space Grant Consortium.

This work is based in part on observations obtained at the Gemini Observatory, which is operated by the Association of Universities for Research in Astronomy, Inc., under a cooperative agreement with the NSF on behalf of the Gemini partnership: the National Science Foundation (United States), the National Research Council (Canada), CONICYT (Chile), Ministério da Ciência, Tecnologia e Inovação (Brazil), and Ministerio de Ciencia, Tecnología e Innovación Productiva (Argentina). S.L.'s research is supported by Gemini Observatory.

Appendix A
Astrometric Measurements of WISE J014656.66+423410.0AB, WISE J053516.80−750024.9, WISEPC J121756.91+162640.2AB, and WISEPC J140518.40+553421

Tables 11–14 give the astrometric measurements of the four Y dwarfs or dwarf systems for which we present new trigonometric parallaxes in Section 7: WISE J014656.66+423410.0AB, WISE J053516.80−750024.9, WISEPC J121756.91+162640.2AB, and WISEPC J140518.40+553421.

Table 11
IRAC Astrometry of WISE J014656.66+423410.0AB

α (J2000) (°)	σ_α (″)	δ (J2000) (°)	σ_δ (″)	MJD
26.7360260	0.017	42.5694192	0.017	55656.09
26.7358510	0.017	42.5694213	0.017	55993.05
26.7357920	0.017	42.5694404	0.017	56215.08
26.7356892	0.017	42.5694181	0.017	56364.26
26.7356867	0.017	42.5694095	0.017	56372.31
26.7356746	0.017	42.5694131	0.017	56388.82
26.7356809	0.017	42.5694104	0.017	56393.13
26.7356172	0.017	42.5694212	0.017	56579.19
26.7356091	0.017	42.5694272	0.017	56592.47
26.7356057	0.017	42.5694355	0.017	56602.48
26.7356033	0.017	42.5694283	0.017	56616.07
26.7355123	0.017	42.5694088	0.017	56737.38
26.7355131	0.022	42.5694102	0.022	56742.07
26.7355103	0.017	42.5694020	0.017	56750.46
26.7355038	0.017	42.5694024	0.017	56758.35
26.7354998	0.017	42.5693956	0.017	56768.07
26.7354985	0.022	42.5694047	0.022	56772.30
26.7354517	0.022	42.5694158	0.022	56947.21
26.7354201	0.022	42.5694134	0.022	56980.00
26.7353199	0.022	42.5693954	0.022	57145.85
26.7352655	0.022	42.5694112	0.022	57340.06

Table 12
IRAC Astrometry of WISE J053516.80−750024.9

α (J2000) (°)	σ_α (″)	δ (J2000) (°)	σ_δ (″)	MJD
83.8199010	0.020	−75.0067327	0.020	55486.25
83.8197269	0.020	−75.0067534	0.020	55668.91
83.8197605	0.020	−75.0067398	0.020	55885.34
83.8195342	0.020	−75.0067408	0.020	56036.95
83.8196093	0.020	−75.0067301	0.020	56264.47
83.8195703	0.020	−75.0067413	0.020	56317.21
83.8194065	0.020	−75.0067341	0.020	56421.97
83.8193712	0.020	−75.0067281	0.020	56450.27
83.8194404	0.020	−75.0067059	0.020	56545.18
83.8194623	0.022	−75.0067298	0.024	56626.48
83.8195022	0.020	−75.0067309	0.020	56641.18
83.8194624	0.020	−75.0067359	0.020	56673.39
83.8192796	0.020	−75.0067386	0.020	56777.50
83.8192769	0.022	−75.0067403	0.024	56780.25
83.8192548	0.020	−75.0067212	0.020	56821.73
83.8192894	0.022	−75.0067191	0.024	56854.02
83.8192649	0.020	−75.0067064	0.020	56875.58
83.8193254	0.022	−75.0067185	0.024	56969.02
83.8191664	0.022	−75.0067402	0.024	57160.80

Table 13
IRAC Astrometry of WISEPC J121756.91+162640.2AB

α (J2000) (°)	σ_α (″)	δ (J2000) (°)	σ_δ (″)	MJD
184.4873562	0.022	16.4443712	0.020	55633.00
184.4875633	0.034	16.4440433	0.037	55972.46
184.4875693	0.022	16.4440330	0.020	55972.47
184.4875799	0.034	16.4440030	0.037	56004.42
184.4876063	0.034	16.4438993	0.037	56131.98
184.4876109	0.022	16.4439086	0.020	56136.37
184.4876155	0.034	16.4438590	0.037	56163.50
184.4880327	0.034	16.4432928	0.037	56741.92
184.4880550	0.034	16.4431730	0.037	56890.37

Table 14
IRAC Astrometry of WISEPC J140518.40+553421.5

α (J2000) (°)	σ_α (″)	δ (J2000) (°)	σ_δ (″)	MJD
211.3259099	0.021	55.5725996	0.020	55583.17
211.3247196	0.031	55.5726728	0.030	55958.16
211.3246853	0.021	55.5726730	0.020	55978.03
211.3245332	0.031	55.5727157	0.030	56026.12
211.3242453	0.031	55.5727649	0.030	56098.29
211.3242425	0.021	55.5727605	0.020	56100.80
211.3239573	0.031	55.5727589	0.030	56169.62
211.3235275	0.021	55.5727358	0.020	56344.47
211.3233998	0.021	55.5727742	0.020	56393.76
211.3232349	0.021	55.5728044	0.020	56435.74
211.3230239	0.021	55.5728328	0.020	56483.50
211.3228253	0.021	55.5728286	0.020	56529.38
211.3223622	0.021	55.5728070	0.020	56718.77
211.3222866	0.031	55.5728223	0.030	56741.77
211.3222193	0.021	55.5728423	0.020	56768.01
211.3220628	0.021	55.5728802	0.020	56810.47
211.3218706	0.021	55.5729028	0.020	56854.10
211.3217215	0.021	55.5728930	0.020	56886.75
211.3216683	0.021	55.5728971	0.020	56902.01
211.3212277	0.031	55.5728659	0.020	57076.29

Appendix B
Online Data Table

Table 15 gives the spectral types, distance moduli, and photometric data used in this work, together with data sources. The table consists of 97 brown dwarfs or brown dwarf systems with spectral types T6 and later.

Table 15
Online Data Table

Column	Units	Explanation
Obj	···	Object Survey+Position+binary-based identifier
SpT	···	Spectral type indicator, e.g., 6 = T6 12 = Y2
$M-m$	mag	Distance modulus, absolute magnitude—apparent magnitude
MJmag	mag	Absolute MKO J (Vega) magnitude
MC2mag	mag	Absolute *Spitzer*/IRAC 4.5 μm (Vega) magnitude
J-C2	mag	MKO J—*Spitzer*/IRAC C2 color
*i*mag	mag	SDSS i (AB) magnitude
*z*mag	mag	SDSS z (AB) magnitude
*Y*mag	mag	MKO Y (Vega) magnitude
*J*mag	mag	MKO J (Vega) magnitude
*H*mag	mag	MKO H (Vega) magnitude
*K*mag	mag	MKO K (Vega) magnitude
L′mag	mag	MKO L' (Vega) magnitude
M′mag	mag	MKO M' (Vega) magnitude
C1mag	mag	*Spitzer*/IRAC 3.6 μm (Vega) magnitude
C2mag	mag	*Spitzer*/IRAC 4.5 μm (Vega) magnitude
C3mag	mag	*Spitzer*/IRAC 5.8 μm (Vega) magnitude
C4mag	mag	*Spitzer*/IRAC 8.0 μm (Vega) magnitude
W1mag	mag	WISE W1 3.35 μm (Vega) magnitude
W2mag	mag	WISE W2 4.6 μm (Vega) magnitude
W3mag	mag	WISE W3 11.6 μm (Vega) magnitude
e_$M-m$	mag	Uncertainty in $M-m$
e_*i*mag	mag	Uncertainty in *i*mag
e_*z*mag	mag	Uncertainty in *z*mag
e_*Y*mag	mag	Uncertainty in *Y*mag
e_*J*mag	mag	Uncertainty in *J*mag
e_*H*mag	mag	Uncertainty in *H*mag
e_*K*mag	mag	Uncertainty in *K*mag
e_*L*′mag	mag	Uncertainty in *L*′mag
e_*M*′mag	mag	Uncertainty in *M*′mag
e_C1mag	mag	Uncertainty in C1mag
e_C2mag	mag	Uncertainty in C2mag
e_C3mag	mag	Uncertainty in C3mag
e_C4mag	mag	Uncertainty in C4mag
e_W1mag	mag	Uncertainty in W1mag
e_W2mag	mag	Uncertainty in W2mag
e_W3mag	mag	Uncertainty in W3mag
Ref1	···	Discovery reference
Comp	···	Name if object is known to be part of a multiple system
Ref2	···	Spectral classification reference
Ref3	···	Trigonometric parallax reference
Ref4	···	Photometry reference

(This table is available in its entirety in machine-readable form.)

References

Ackerman, A. S., & Marley, M. S. 2001, ApJ, 556, 872
Allard, N. F., Allard, F., & Kielkopf, J. F. 2005, A&A, 440, 1195
Althaus, L. G., Serenelli, A. M., Panei, J. A., et al. 2005, A&A, 435, 631
Baraffe, I., Chabrier, G., Barman, T. S., Allard, F., & Hauschildt, P. H. 2003, A&A, 402, 701
Beamin, J. C., Ivanov, V. D., Bayo, A., et al. 2014, A&A, 570, L8
Beichman, C., Gelino, C. R., Kirkpatrick, J. D., et al. 2014, ApJ, 783, 68
Bensby, T., Feltzing, S., Lundstrom, I., & Ilyin, I. 2005, A&A, 433, 185
Bensby, T., Feltzing, S., & Oey, M. S. 2014, A&A, 562, 71
Bouvier, J., Matt, S. P., Mohanty, S., et al. 2014, in Protostars and Planets VI, ed. H. Beuther et al. (Tucson, AZ: Univ. Arizona Press), 433
Burgasser, A. J., Kirkpatrick, J. D., Brown, M. E., et al. 2002, ApJ, 564, 421
Burgasser, A. J., Looper, D., & Rayner, J. T. 2010, AJ, 139, 2448
Burrows, A., Marley, M. S., Hubbard, W. B., et al. 1997, ApJ, 491, 856
Burrows, A., Sudarsky, D., & Lunine, J. I. 2003, ApJ, 596, 587
Covey, K. R., Ivezic, Z., Schlegel, D., et al. 2007, AJ, 134, 2398
Cushing, M. C., Hardegree-Ullman, K. K., Trucks, J. L., et al. 2016, ApJ, 823, 152
Cushing, M. C., Kirkpatrick, J. D., Gelino, C. R., et al. 2011, ApJ, 743, 50
Cushing, M. C., Kirkpatrick, J. D., Gelino, C. R., et al. 2014, AJ, 147, 113
Davenport, J. R. A., Ivezic, Z., Becker, A. C., et al. 2014, MNRAS, 440, 3430
Delorme, P., Delfosse, X., Albert, L., et al. 2008, A&A, 482, 961
Dufour, P., Bergeron, P., & Fontaine, G. 2005, ApJ, 627, 404
Dupuy, T. J., & Kraus, A. L. 2013, Sci, 341, 1492
Dupuy, T. J., & Liu, M. C. 2012, ApJS, 201, 19
Dupuy, T. J., Liu, M. C., & Leggett, S. K. 2015, ApJ, 803, 102
Eikenberry, R., Elston, R., Guzman, R., et al. 2004, Proc. SPIE, 5492, 1196
Elias, J. H., Joyce, R. R., Liang, M., et al. 2006, Proc. SPIE, 6269, 138
Esplin, T. L., & Luhman, K. L. 2016, AJ, 151, 9
Esplin, T. L., Luhman, K. L., Cushing, M. C., et al. 2016, ApJ, 832, 58
Faherty, J. K., Beletsky, Y., Burgasser, A. J., et al. 2014, ApJ, 790, 90
Freedman, R. S., Lustig-Yaeger, J., Fortney, J. J., et al. 2014, ApJS, 214, 25
Freytag, B., Allard, F., Ludwig, H.-G., Homeier, D., & Steffen, M. 2010, A&A, 513, 19
Geballe, T. R., Saumon, D., Golimowski, D. A., et al. 2009, ApJ, 695, 844
Golimowski, D. A., Leggett, S. K., Marley, M. S., et al. 2004, AJ, 127, 3516
Helling, Ch., Oevermann, M., Luttke, M. J. H., Klein, R., & Sedlmayr, E. 2001, A&A, 376, 194
Hodapp, K. W., Jensen, J. B., Irwin, E. M., et al. 2003, PASP, 115, 1388
Hubeny, I., & Burrows, A. 2007, ApJ, 669, 1248
Kirkpatrick, J. D., Cushing, M. C., Gelino, C. R., et al. 2011, ApJS, 197, 19
Kirkpatrick, J. D., Cushing, M. C., Gelino, C. R., et al. 2013, ApJ, 776, 128
Kirkpatrick, J. D., Gelino, C. R., Cushing, M. C., et al. 2012, ApJ, 753, 156
Knapp, G. R., Leggett, S. K., Fan, X., et al. 2004, AJ, 127, 3553
Lawlor, T. M., & MacDonald, J. 2006, MNRAS, 371, 263
Leggett, S. K., Currie, M. J., Varricatt, W. P., et al. 2006, MNRAS, 378, 781
Leggett, S. K., Cushing, M. C., Hardegree-Ullman, K. K., et al. 2016a, ApJ, 830, 141
Leggett, S. K., Cushing, M. C., Saumon, D., et al. 2009, ApJ, 695, 1517
Leggett, S. K., Hawarden, T. G., Currie, M. J., et al. 2003, MNRAS, 345, 144
Leggett, S. K., Liu, M. C., Dupuy, T. J., et al. 2014, ApJ, 780, 62
Leggett, S. K., Morley, C. V., Marley, M. S., et al. 2013, ApJ, 763, 130
Leggett, S. K., Morley, C. V., Marley, M. S., & Saumon, D. 2015, ApJ, 799, 37
Leggett, S. K., Saumon, D., Marley, M. S., et al. 2007, ApJ, 655, 1079
Leggett, S. K., Saumon, D., Marley, M. S., et al. 2012, ApJ, 748, 74
Leggett, S. K., Tremblin, P., Saumon, D., et al. 2016b, ApJ, 824, 2
Liu, M. C., Dupuy, T. J., Bowler, B. P., Leggett, S. K., & Best, W. M. J. 2012, ApJ, 758, 57
Liu, M. C., Leggett, S. K., & Chiu, K. 2007, ApJ, 660, 1507
Lodders, K., & Fegley, B. 2002, Icar, 155, 393
Lucas, P. W., Tinney, C. G., Burningham, B., et al. 2010, MNRAS, 408, L56
Luhman, K. L. 2014, ApJL, 786, L18
Luhman, K. L., Burgasser, A. J., & Bochanski, J. J. 2011, ApJL, 730, L9
Luhman, K. L., & Esplin, T. L. 2016, AJ, 152, 78
Luhman, K. L., Morley, C. V., Burgasser, A. J., Esplin, T. L., & Bochanski, J. J. 2014, ApJ, 794, 16
Marley, M. S., Saumon, D., Cushing, M., et al. 2012, ApJ, 754, 135
Marley, M. S., Saumon, D., & Goldblatt, C. 2010, ApJL, 723, L11
Marsh, K. A., Wright, E. L., Kirkpatrick, J. D., et al. 2013, ApJ, 762, 119
McMahon, R. G., Banerji, M., Gonzalez, E., et al. 2013, Msngr, 154, 35
Morley, C. V., Fortney, J. J., Marley, M. S., et al. 2012, ApJ, 756, 172 (M12)
Morley, C. V., Marley, M. S., Fortney, J. J., et al. 2014, ApJ, 787, 78 (M14)
Noll, K. S., Geballe, T. R., & Marley, M. S. 1997, ApJL, 489, L87
Opitz, D., Tinney, C. G., Faherty, J. K., et al. 2016, ApJ, 819, 17
Pickles, A. J. 1998, PASP, 110, 863
Pinfield, D. J., Burningham, B., Lodieu, N., et al. 2012, MNRAS, 422, 1922
Pinfield, D. J., Gromadzki, M., Leggett, S. K., et al. 2014, MNRAS, 444, 1931
Radigan, J., Jayawardhana, R., Lafreniere, D., et al. 2012, ApJ, 750, 105
Rayner, J. T., Cushing, M. C., & Vacca, W. D. 2009, ApJS, 185, 289
Rodriguez, D. R., Zuckerman, B., Melis, C., & Song, I. 2011, ApJL, 732, L29
Saumon, D., Geballe, T. R., Leggett, S. K., et al. 2000, ApJ, 541, 374
Saumon, D., & Marley, M. S. 2008, ApJ, 689, 1327
Saumon, D., Marley, M. S., Abel, M., Frommhold, L., & Freedman, R. S. 2012, ApJ, 750, 74 (S12)
Saumon, D., Marley, M. S., Cushing, M. C., et al. 2006, ApJ, 647, 552
Saumon, D., Marley, M. S., Leggett, S. K., et al. 2007, ApJ, 656, 1136
Schneider, A. C., Cushing, M. C., Kirkpatrick, D. J., & Gelino, C. R. 2016, ApJL, 823, 35
Schneider, A. C., Cushing, M. C., Kirkpatrick, J. D., et al. 2015, ApJ, 804, 92
Skemer, A. J., Morley, C. V., Allers, K. N., et al. 2016, ApJL, 826, L17
Skrzypek, N., Warren, S. J., & Faherty, J. K. 2016, A&A, 589, 49
Stephens, D. C., Leggett, S. K., Cushing, M. C., et al. 2009, ApJ, 702, 154

Subasavage, J. P., Jao, W.-C., Henry, T. J., et al. 2009, AJ, 137, 4547
Tinney, C. G., Faherty, J. K., Kirkpatrick, J. D., et al. 2012, ApJ, 759, 60
Tinney, C. G., Faherty, J. K., Kirkpatrick, J. D., et al. 2014, ApJ, 796, 39
Tokunaga, A. T., & Vacca, W. D. 2005, PASP, 117, 421
Tremblin, P., Amundsen, D. S., Chabrier, G., et al. 2016, ApJL, 817, L19
Tremblin, P., Amundsen, D. S., Mourier, P., et al. 2015, ApJL, 804, L17 (T15)
Tsuji, T., Ohnaka, K., Aoki, W., & Nakajima, T. 1996, A&A, 308, L29
Visscher, C. 2012, LPI, 1675, 8046
Visscher, C., Lodders, K., & Fegley, B. 2006, ApJ, 648, 1181
Visscher, C., & Moses, J. I. 2011, ApJ, 738, 72
Wang, D., Gierasch, P. J., Lunine, J. I., & Mousis, O. 2015, Icar, 250, 154
Warren, S. J., Mortlock, D. J., Leggett, S. K., et al. 2007, MNRAS, 381, 1400
Wright, E. L., Eisenhardt, P. R. M., Mainzer, A. K., et al. 2010, AJ, 140, 1868
Yurchenko, S. N., Barber, R. J., & Tennyson, J. 2011, MNRAS, 413, 1828
Yurchenko, S. N., & Tennyson, J. 2014, MNRAS, 440, 1649
Zahnle, K. J., & Marley, M. S. 2014, ApJ, 797, 41
Zapatero Osorio, M. R., Lodieu, N., Béjar, V. J. S., et al. 2016, A&A, 592, 80